# Large Eddy Simulation of an Arctic Mixed-Phase Boundary Layer Cloud

Matti Räsänen
Master Thesis
Environmental Engineering
Department of Applied Physics
University of Eastern Finland

University of Eastern Finland, Faculty of Science and Forestry
Environmental Engineering
Matti Räsänen: Large Eddy Simulation of an Arctic Mixed-Phase Boundary Layer Cloud

Master Thesis 67 pages
Supervisors: Sami Romakkaniemi and Harri Kokkola
May 2012
Keywords: Atmospheric boundary layer, Mixed-phase cloud, Large eddy simulation.

**Abstract:** Representation of the clouds in all kinds of numerical models of the atmosphere is a major challenge. Not even the small scale high-resolution models can capture all the known cloud physics and thus various parametrizations have to be used. The problem is further complicated when ice phase is studied. In this thesis, an overview is given of the modeling of the atmospheric boundary layer using a LES model with a special emphasis on the ice microphysics. UCLA LES model was used to study an Arctic mixed-phase boundary layer cloud that was measured during the First ISCCP Regional Experiment – Arctic Cloud Experiment (FIRE-ACE) on May 7th, 1998. The UCLA LES model did not include ice microphysics so a simplified version of the Seifert and Beheng 2-moment bulk microphysics scheme with ice crystal phase was implemented into the model. Also a parametrization of radiative properties of the ice crystal was implemented to the existing 2-dimensional delta-four-stream radiation scheme. The ice crystals were assumed to be hexagonal plates.

In the simulations, sensitivity to the ice nuclei (IN) concentration was tested using prescribed values of $N_{IN}$=0 m$^{-3}$, $N_{IN}$=170 m$^{-3}$, $N_{IN}$=1700 m$^{-3}$ and $N_{IN}$=5100 m$^{-3}$. Comparing these results two different states were observed in the end of the simulations: one with a stable mixed-phase cloud and the other with an all-ice cloud. The radiative properties confirmed the fact that ice clouds are optically thinner than warm phase clouds. Further study is needed especially focusing on the ice nucleation which is not yet well understood.

**Tiivistelmä:** Pilvien esittäminen numeerisissa ilmakehämalleissa on suuri haaste. Pienenkään mittakaavan tarkat mallit eivät pysty kuvaamaan kaikkia pilvifysiikan ilmiöitä. Tästä johtuen joudutaan tekemään parametrisaatioita kyseisistä ilmiöistä. Jääpilviä tutkittaessa ongelma on vielä monimutkaisempi. Tässä työssä esitellään ilmakehän rajakerroksen mallintamista isopyörresimulaation avulla keskittyen erityisesti jään mikrofysiikkaan. Työssä käytettiin UCLA LES –mallia, jonka avulla tutkittiin arktista monifaasi pilveä, joka oli mitattu FIRE-ACE (First ISCCP Regional Experiment – Arctic Cloud Experiment) mittauskamppanjan aikana 7. päivä toukokuuta 1998. UCLA LES –malli ei sisältänyt jään mikrofysiikkaa, joten yksinkertaistettu versio Seifertin ja Behengin kahden momentin bulk mikrofysiikasta toteutettiin jääkiteille. Jääkiteiden oletettiin olevan kuusikulmion muotoisia.

Simulaatioiden herkkyyttä jääytimien lukumäärä konsentraatioon testattiin arvoilla $N_{IN}$=0 m$^{-3}$, $N_{IN}$=170 m$^{-3}$,$N_{IN}$=1700 m$^{-3}$ ja $N_{IN}$=5100 m$^{-3}$ Vertailemalla saatuja tuloksia havaittiin kaksi erilaista lopputulosta: toisessa syntyi stabiili monifaasi pilvi ja toisessa syntyi pelkästään jäästä koostuva pilvi. Vertailemalla pilvien säteilyominaisuuksia havaittiin, että jääpilvet ovat optisesti harvempia kuin nestepilvet. Lisätutkimuksia tarvitaan erityisesti jääytimien nukleaatiosta, joka on vielä heikosti ymmärretty ilmiö.

## Acknowledgments

This work was carried out during an internship in the summer 2011 and subsequent months while working and studying in the department of aerosol physics at the University of Eastern Finland.

I would like to thank my supervisors Sami Romakkaniemi and Harri Kokkola for continuous support during the work which at times was not progressing as expected. I would also like to thank Zubair Maalick for valuable discussions related to the work.

The atmosphere at the department was encouraging and I would like to thank all the people of the aerosol science group. Special thanks goes to Alex for rigorous discussion of the numerical methods. Thanks also to Björn Stevens for making the UCLA LES code free software without which this work could not have been done.

Last but not least I would like to thank my parents, friends and my girlfriend Marinka for the support that I much needed.

In Kuopio on May 2012
Matti Räsänen

# Contents

# 1 Introduction

In the recent years, weather and climate has become under increasing study. Weather affects our daily life and climate change is one of the greatest social, economic and environmental challenges of our time. Thus, it is of crucial importance to study the Earth's atmosphere.

Clouds are an essential part of the atmosphere. A cloud consists of visible aggregate of tiny water droplets and/or ice particles. Clouds distribute the solar heat and moisture over the Earth's surface and provide vital precipitation. Clouds and aerosols, which are the smallest particles in the atmosphere are not yet well represented in the large scale General Circulation Models (GCM) which cover the surface and atmosphere of the Earth as well as the oceans. These models are used to make predictions of the future climate of the Earth. In the latest IPCC report it is stated that representation of clouds and the effects of aerosols on clouds are the major uncertainties in the current models [1]. This uncertainty arises mainly due to the fact that a small perturbations in the cloud processes can have significant effect in the large scale, and due to various phases and forms that water can have in the atmosphere.

There are many types of clouds which all have their unique way to form and evolve in time. Cloud types are divided by their height range into high, middle and low level clouds. From the low level clouds stratocumulus and cumulus clouds are the most frequently studied clouds and they are the most abundant clouds in the atmosphere.

Clouds and atmosphere can be studied using numerical simulations of various spatial scales. Smallest scale direct numerical simulations (DNS) solve the flow field explicitly and have domain of few meters. Typically these models are used to study the edges of the clouds. To extend the computational domain, Large Eddy Simulation(LES) has to be used. In a LES model, most of the kinetic energy of the atmospheric flow is calculated explicitly giving a very detail information of the flow. This kind of model combined with observations is the basis for the parametrizations of boundary layer and clouds in the large scale models. LES model is an ideal tool for detailed modeling of lower levels of atmosphere but it is too heavy for weather forecasting, which can be done using mesoscale models. As an example of a mesoscale model is the HIRLAM model which is used in numerical weather forecasting in Finland [2]. In large scale modeling, the general circulation models are used for numerical weather forecasting as well as predicting the future climate on the Earth.

This study focused on the Arctic boundary layer clouds. It has been shown that the Arctic has warmed at roughly twice the global average rate since the preindustrial period, and that the trend is expected to continue during this century [3]. Further, it has been shown that the GCMs have large discrepancies in predictions of present and future climate in the Arctic which leads to large uncertainties in the global climate change predictions [4]. Numerous simulations of the Arctic boundary layer have been done [5] [6] [7] [8]. Recently, it has become customary to evaluate the results from simulations with observations by doing an LES-intercomparison study in which different models are run with identical initial conditions [9] [10]. In this kind of study the models can be compared and the sources of uncertainties can be understood better.

In this study, the UCLA LES model which has been used before to study stratocumulus and cumulus clouds, was used to study an Arctic stratus cloud. The model was extended to include a simplified version of the Seifert and Beheng 2-moment bulk microphysics scheme with ice crystal phase and a parametrization of the radiative properties of ice crystals. In the simulations, an Arctic mixed-phase boundary layer cloud was studied focusing on the sensitivity of the ice nuclei concentration to the cloud.

## 1.1 Arctic boundary layer

The area of this study is the atmospheric boundary layer, which is defined as the lowest layer of atmosphere that is directly influenced by the presence of the Earth's surface and responds to surface forcings with a timescale of about an hour or less [11]. The boundary layer depth ranges from few hundred meters to 3 km. The layer between the boundary layer and tropopause is called free troposphere. Boundary layer has different type of characteristics depending on the latitude and the surface below it. In a mid-latitude boundary layer over land the dominant forcings are the diurnal cycle and the large scale synoptic forcings, whereas in the summertime Arctic boundary layer the diurnal variations in the clouds are slight [11] [12].

This study focuses on the simulation of the Arctic boundary layer. In it low-level stratiform cloud are common in the summertime. Monthly average cloud cover amounts are nearly 70% between May and September [13]. In contrast to mid-latitude boundary layer clouds, the Arctic boundary layer clouds can have multiple levels, which has been a difficult special case to model with the LES models [14]. Mixed-phase clouds, which consist of liquid water and ice, occur during spring and autumn. In the Arctic boundary layer extremely stable conditions may persist for many weeks leading to decoupling of the surface from the free atmosphere [15]. In essence, Arctic clouds are predominantly optically thin and low lying clouds.

Arctic has attracted explorers and scientists for a long time and in recent years there have been more measuring campaigns focusing on it. Some of the recent campaigns are introduced here briefly.

It has been a difficult task to make observations in the Arctic because of long polar nights, extreme cold, and lack of permanent measurement sites. It is fair to say that in the Arctic the interactions of clouds, atmosphere and the ocean/sea ice surface exhibit a highly complex system for which the processes and interactions are less well understood than the phenomena in lower latitude. In Table 1 there are recent experiments and their goals in trying to understand better the Arctic.

Table 1: Name and goal of recent measuring experiments in the Arctic.

| Abbreviation | Goal of the study |
|---|---|
| ASCOS | Arctic Summer Cloud Ocean Study. Studies the formation of cloud condensation and ice nuclei in low level cloud systems over the Arctic pack ice (2008) [16]. |
| ARM | Atmospheric Radiation Measurement. Long-term measurements near Barrow, Alaska (since 1994) [17]. |
| ISDAC | Indirect and Semi-Direct Aerosol Campaign. Focused on the aerosol effects on clouds and radiative forcing (2008) [18]. |
| FIRE-ACE | First International Satellite Cloud Climatology Project Regional Experiment - Arctic Clouds Experiment. Aircraft observations of radiation exchange between the surface, atmosphere, and space, and to study how the surface influences the evolution of boundary layer clouds (1998) [19]. |
| M-PACE | Mixed-Phase Arctic Cloud Experiment. Focused on dynamics, microphysics and radiative properties (2004) [20]. |
| SHEBA | Surface Heat Budget of the Arctic Ocean Experiment. Focused on understanding and predicting the physical processes that determine the surface energy budget and the sea–ice mass balance in the Arctic (1997) [21]. |

From these campaigns, SHEBA, FIRE-ACE and ARM, is a group of interdependent field programs that have gathered data which has been used to come up with a more realistic representation of the processes controlling the atmosphere in the Arctic. The campaigns have also lead to modeling studies, which aim to incorporate these representations into the large-scale models. These studies will lead to a much more complete understanding of the total sensitivity of the Arctic air–sea–ice system to variations in atmospheric and oceanic forcing on seasonal, inter annual and longer timescales.

The M-PACE campaign focused specifically on the study of mixed-phase stratus clouds during autumn and their dynamics, microphysics and radiative properties. The most recent campaigns are ISDAC and ASCOS. ISDAC aims to improve our knowledge on how the changes in the composition and concentration of aerosols influence cloud properties and the associated radiative forcing. ASCOS is an interdisciplinary study of some of the controlling factors of the low-level cloud system, especially the formation of cloud condensation and ice nuclei, over the Arctic pack ice.

## 1.2 Ice phase physics

Clouds can be divided into "warm" clouds and "cold" clouds. This means that former consist of water vapor and liquid water whereas the latter also consist of ice. The microphysical processes that govern the warm phase clouds have been studied extensively and their details are much better understood compared to the cold clouds.

Cloud ice microphysics is complicated because of the various forms and shapes of ice crystals and the processes that control these shapes. Observed ice phases in clouds include ice crystals, snow, graupel, and hail. These range in size from 1 µm to $10 \times 10^5$ µm [22]. These groups can further be divided into different categories based on their size and density. In terms of shape, the ice crystals can have almost an unlimited range of shapes as can be observed from the falling ice crystals from the sky. The primary controlling factors for ice crystal formation is the ambient temperature and supersaturation with respect to ice. In the Figure 3, the shape of the ice crystals is shown as a function of ambient temperature and ice supersaturation.

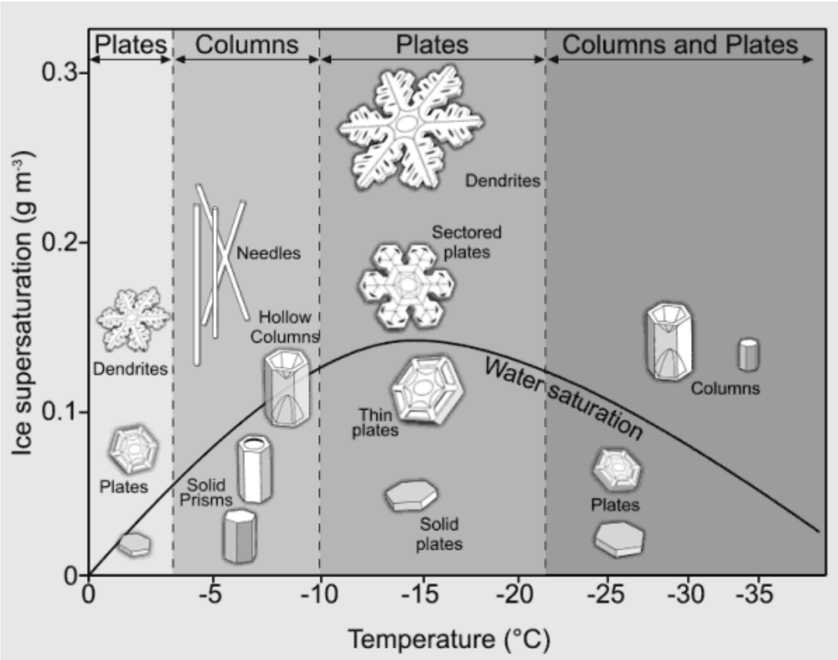


Figure 1: The shape of ice crystals as a function of both ambient temperature and ice supersaturation [23].

The evolution of an ice particle starts by ice nucleation in which an ice particle is formed by ice forming around a small ice nuclei (IN). Here, and from now on, ice is defined as water in its ice phase. Many substances like soot, minerals and organic compounds can act as an ice nuclei which originate from natural and anthropogenic sources. At first ice grows mainly due to water vapor deposition and later it starts to collect other particles in different kinds of collision and coalescence processes. One of them is riming in which the ice crystal is growing by collecting small water droplets. Graupel and hail are initiated from rimed crystals and all these phases can collide with each other and form new aggregates. In addition, ice particles can melt and liquid water can freeze to form ice crystals [12]. Many of these processes are functions of terminal fall speed of the particle, which in turn can have values ranging from 0 to 25 $\mathrm{m\,s^{-1}}$. To illustrate the terminal fall speed relationship for the different ice particles Figure 2 shows the mass-weighted mean fall speed as a function of mixing ratio for different types of particles. Particles with lower density, like snow and aggregates, have lower fall speed than nearly solid-ice hail particles.

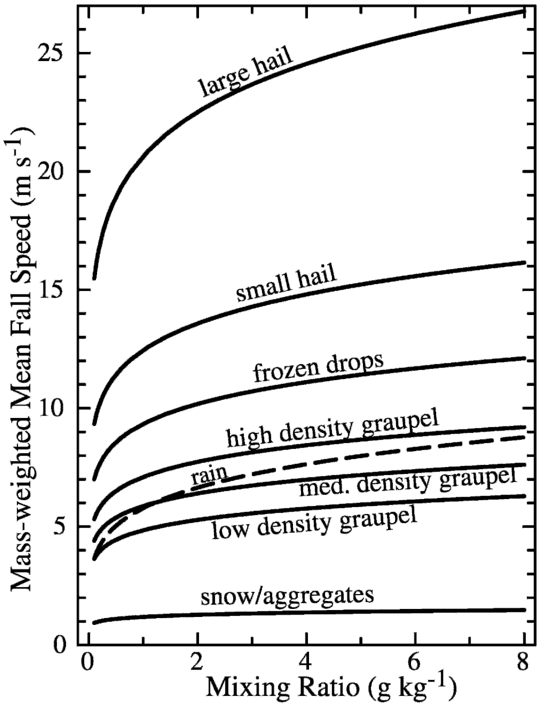


Figure 2: Mass-weighted mean terminal fall speed as function of mixing ratio for different types of ice particles [24].

Many of the observed ice microphysical processes such as nucleation, depositional growth, riming, collision/coalescence, freezing and melting are now incorporated in to the current models, although inadequate basic knowledge about the process kinetics has tended to restrict their complete and appropriate application [22].

When simulating the clouds on a computer the cloud microphysical processes have to be simplified further because an explicit prediction of all the characteristics of the clouds is impractical. A simple parametrization which captures the essence of the known microphysical processes is used as an alternative to the explicit calculation [12]. This means that there are two primary sources of error in the cloud models: either the physics of the clouds is not well enough known or the simple parametrization does not capture all the know physics.

## 1.3 Radiative properties

All energy that reaches the Earth comes from the Sun. The absorption and loss of radiant energy by the Earth and the atmosphere are totally responsible for the Earth's weather on both global and local scales [25]. It has been measured that the average temperature on the Earth remains fairly constant meaning that the Earth and the atmosphere on the whole lose as much energy by radiation back into space as is received by radiation from the Sun. Although the absorption of the solar radiation takes place mostly at the surface of the Earth, the atmosphere controls the amount of solar radiation that reaches the surface of the Earth, and, at the same time, controls the amount of the outgoing terrestrial radiation that escapes into space.

The Earth's atmosphere is mainly composed of nitrogen, oxygen and argon accounting 99.96 % of the volume with nearly constant concentrations. The rest of the atmosphere is composed of some gases that have nearly permanent concentrations and trace gases which concentrations vary in space and time. The atmosphere also contains various kinds of aerosols, clouds and precipitation, which are highly variable in space and time.[26]

Clouds absorb and scatter the incoming solar radiation as well as absorb and emit thermal infrared radiation. The radiant energy, arranged in order of its wavelengths $\lambda$, is the energy spectrum of radiation. Although the Sun radiates X-rays, ultraviolet, visible light and infrared radiation most of the energy is concentrated on wavelengths from 0.2 µm to 4 µm [27]. The thermal infrared radiation from the Earth spans from 4 µm to 100 µm. These are also called the shortwave (SW) and longwave (LW) radiations, respectively. The effect of clouds on radiation is primarily related to the vertical distribution of condensate in the cloud. Precipitation alters this vertical distribution of condensate and this way affects the radiative properties of clouds. Also the phase change from liquid water to ice changes the radiative properties. Furthermore, ice can affect the rate of absorption of solar radiation which, in turn, can alter the thermodynamic stability of the cloud.

In the Arctic radiation is complicated particularly because of highly reflecting snow and ice, low temperatures and water vapor amounts [13]. The surface albedo is especially important variable because it controls the amount of absorbed solar radiation, which in turn determines the rate of melting of ice. Globally, clouds have a net cooling effect on the Earth-atmosphere system. However, Arctic stratus clouds have a net warming effect on the surface during the winter and a net cooling effect on the surface during the summer. This is because during the winter, there is no solar radiation.

## 1.4 Outline

In this thesis a general introduction to the methodology for modeling clouds is presented with emphasis on the ice microphysical processes and radiative properties.

The following chapter introduces the dynamical and thermodynamical principles of the atmosphere. It also has a summary of the UCLA LES model. In Chapter 3, parts of the Seifert and Beheng two-moment microphysical scheme are presented. In Chapter 4 the radiative transfer equation, that was used in the model, is derived and the ice crystal parametrization added to model is presented. Results of the simulations are presented in the Chapter 5 and conclusions are made in Chapter 6.

An effort has been made to make the text readable and consistent. All notations including the variable names and operators are kept consistent throughout the text and are given in Appendix A.

# 2 Modeling

In this chapter the basics of dynamics and thermodynamics governing the boundary layer are presented. This topic is wide and a very detailed approach is beyond the scope of this thesis. In the following chapters only the most important and relevant parts of the theory are presented with emphasis on methods that have been used in the UCLA LES model. The main point is to introduce the variables that will be used later to analyze the results of the simulations. The UCLA LES model is over 10000 lines of code so it cannot be covered in detail. Instead, in the end of the chapter a summary of the methods with appropriate references are given.

## 2.1 Thermodynamics

Thermodynamics of air can be categorized into three groups: dry air, unsaturated moist air and saturated moist air thermodynamics. Dry air thermodynamics and unsaturated moist air thermodynamics differ in the sense that the effective heat capacities are influenced by the presence of water vapor. Additionally, saturated moist air thermodynamics involves phase changes which introduces a variety of new dynamical processes with no analogs in dry air thermodynamics. In this chapter the variables for dry air and moist air thermodynamics are presented while some of the processes involving phase changes are discussed in Chapter 3. This division is due to the usual way in which the problems of condensation, sublimation, freezing and precipitation are considered to be a part of cloud microphysics.

There are different variables to represent the amount of water vapor in the air. One way to represent it is by mixing ratios, which is done here because the UCLA LES model also uses them. Mixing ratio $r$ can be defined as

$$r = \frac{m}{m_d}, \tag{2.1}$$

where $m$ is the mass of the substance per unit volume and $m_d$ is the mass of dry air per unit volume [28]. Using this definition water vapor mixing ratio $r_v$, liquid water mixing ration $r_l$, and ice water mixing ratio $r_i$, can be defined by replacing the $m$ with the mass of appropriate substance. Total water mixing ratio can be defined as

$$r_t = r_v + r_l, \tag{2.2}$$

It is an important quantity which is usually nearly constant in the boundary layer although microphysical processes can alter it. Liquid water mixing ratio is the other important variable which is used to define the cloud in simulations. Examples of the evolution of these variables during simulations are presented later in the Chapter 5.2.

In addition to the pressure $p$, a non-dimensional exner function can be defined as

$$\Pi = \left(\frac{p}{p_{00}}\right)^{\frac{R_d}{c_p}}, \tag{2.3}$$

where $p_{00}$ is a constant reference pressure of 1000 mb, $R_d$ is the gas constant for dry air and $c_p$ is the heat capacity of dry air in constant pressure [29]. Using the exner function, potential temperature can be defined as

$$\theta = \frac{T}{\Pi}, \tag{2.4}$$

where $T$ is the absolute temperature. Potential temperature is the temperature that air would have if brought isentropically to the pressure $p_{00}$. This is the temperature used to define the thermodynamic state of dry air because it is conserved in adiabatic displacements of unsaturated air [30]. It does not take into account the presence of water, so another useful modified temperature is the virtual potential temperature for saturated air

$$\theta_v = \theta\,(1 + (\frac{R_v}{R_d} - 1)r_t - r_l). \tag{2.5}$$

where $R_v$ is the gas constant for water vapor [11]. It can be shown that fluctuations in the virtual potential temperature have same role as the density fluctuations. Thus virtual potential temperature can be used to define the buoyancy which changes depending on the amount of water. Water vapor decreases the average density of air, increasing buoyancy, while the presence of liquid water increases the density of air, thus decreasing buoyancy. In the UCLA LES model buoyancy is defined as

$$B = g \times \left(\frac{\theta(1 + 0.61r_v) - \Theta_0}{\Theta_0} - r_l - r_r - r_i\right), \tag{2.6}$$

where $r_r$ is the rain water mixing ratio and $\Theta_0$ is the basic state value of the potential temperature which depends only on the height.

The pressure perturbations in the UCLA LES model are handled in two separate pressures, $\pi_0$ and $\pi_1$. The anelastic approximation solves for perturbations about a hydrostatic basic state of constant potential temperature as follows

$$\frac{\mathrm{d}\pi_0}{\mathrm{d}z} = -\frac{g}{c_p\Theta_0}. \tag{2.7}$$

The second pressure depends on time and is updated in the code by finding the pressure that balances the mean accelerations, such that

$$\frac{\mathrm{d}\pi_1}{\mathrm{d}z} = \Theta_0\bar{w}, \tag{2.8}$$

where $\bar{w}$ is the average vertical velocity and $\pi_1 = 0$ when $z = 0$. These pressures are adjusted as follows

$$\frac{\mathrm{d}}{\mathrm{d}z}(\pi_0 + \pi_1) = -\frac{g}{c_p\bar{\theta}_v}. \tag{2.9}$$

Another temperature has to be defined to account for the moist equivalent of the potential temperature. There are two choices: either all water is assumed to be in vapor state or in liquid state. In the UCLA LES model the liquid water potential temperature is defined as

$$\theta_l = \theta \exp\left(-\frac{L_v}{c_pT}r_l\right), \tag{2.10}$$

where $L_v$ is the latent heat of vaporization. This temperature can be interpreted as an evaporation temperature and in the absence of liquid water, it reduces to the potential temperature. On the other hand, in saturated conditions, the difference between $\theta_l$ and $\theta$ expresses the enthalpy of vaporization released through the formation of any condensate. Finally for moist air thermodynamics, the thermodynamic state is completely defined using the variables $\theta_l$,$r_t$ and $p$.[31]

Another set of variables are defined to describe the overall amount of condensate. These are the Liquid Water Path (LWP), Rain Water Path (RWP) and Ice Water Path (IWC) defined as

$$\mathrm{LWP} = \int_0^{z_t} \rho_{air} r_l \mathrm{d}z, \tag{2.11a}$$

$$\text{RWP} = \int_0^{z_t} \rho_{air} r_r \mathrm{d}z, \tag{2.11b}$$

$$\text{IWP} = \int_0^{z_t} \rho_{air} r_i \mathrm{d}z, \tag{2.11c}$$

where $z_t$ is the cloud top height [11]. They represent the weight of condensate above a unit surface area on the Earth and can be obtained from satellite measurements.

## 2.2 Physical principles

To describe the equations governing the motion in the atmosphere, the conservation laws of mass, momentum and energy are written. This set of equations is so complex that no analytical solution is known and only approximate numerical solution can be found. Numerical methods are not covered here but the numerical methods used in the UCLA LES model, are listed in the Chapter 2.4.

Starting from conservation of mass which can be written as

$$\frac{\partial \rho}{\partial t} + \frac{\partial \rho u_j}{\partial x_j} = 0, \tag{2.12}$$

where $\rho$ is the density of air, x represents the Cartesian coordinates $(x_1,x_2,x_3)$=(x,y,z) and $u_j$ represents the velocity in the direction $x_j$. A shorthand Einstein summation notation is used which implicitly assumes summation over the index j [11]. Conservation of momentum is expressed in the Navier-Stokes equations which is an expression of Newton's second law of motion for a fluid of constant density [32]. For vector $\vec{u}$ Navier-Stokes equation is

$$\rho \frac{\mathrm{D}\vec{u}}{Dt} = -\nabla p + \mu_{vis} \nabla^2 \vec{u} + \vec{F}. \tag{2.13}$$

which in summation notation is equivalently written as

$$\rho \left( \frac{\partial u_i}{\partial t} + \frac{\partial u_j u_i}{\partial u_j} \right) = -\frac{\partial p}{\partial x_i} + \frac{\partial}{\partial x_j} \left( \mu_{vis} \frac{\partial u_i}{\partial x_j} \right) + F_{ijk}, \tag{2.14}$$

where $\mu_{vis}$ is the coefficient of viscosity, p is pressure and $F_{ijk}$ denotes the body forces acting on a parcel of air. The main body forces are gravitational force and Coriolis force. Gravitational force is defined as

$$F_{i,grav} = -\delta_{i3}\rho g, \text{ where } \delta_{ij} = \begin{cases} 0 & \text{for } i \neq j \\ 1 & \text{for } i = j \end{cases} \tag{2.15}$$

where g is acceleration due to gravity and $\delta_{ij}$ is the Kronecker delta. The Coriolis force due to the Earth's rotation is defined as

$$F_{ijk,coriolis} = 2\epsilon_{ijk}\Omega_j u_k \tag{2.16}$$

where $\Omega$ is the Earth's angular velocity and Levi-Civita symbol $\epsilon_{ijk}$ is defined as

$$\epsilon_{ijk} = \begin{cases} +1 & \text{if (i,j,k) is (1,2,3),(3,1,2) or (2,3,1)} \\ -1 & \text{if (i,j,k) is (1,3,2),(3,2,1) or (2,1,3)} \\ 0 & \text{if i=j or j=k or k=i.} \end{cases} \tag{2.17}$$

The conservation of the scalar variables $r_t$, $\theta_l$ and the microphysical variables have general form of

$$\frac{\partial \varphi}{\partial t} + \frac{\partial \varphi u_j}{\partial x_j} = S_\varphi \tag{2.18}$$

where $\varphi$ is the specific scalar variable and $S_\varphi$ includes the source/sink terms of a specific scalar variable [33]. For $r_t$ and $\theta_l$, the source/sink terms include the effect of freezing/melting, radiation and precipitation. The exact parametrized equations for the microphysical variables are presented in Sec. 3.6.

## 2.3 LES filtering and approximations

The Large Eddy Simulation (LES) approach can be used to derive the approximate equations of motion. This technique involves a LES filter function which is used to filter the Navier-Stokes equation so that sub-grid scale solutions are eliminated. Those motions are parametrized by the sub-grid model using known quantities. There are many ways to parametrize the sub-grid scale motion and in UCLA LES the Smagorinsky model is used.

To make the Large Eddy Simulation (LES) approximation we have to define a filtering operator for the governing equations.

$$\widetilde{\varphi}(\vec{x}, t) = \int G(\vec{r}, \vec{x})\varphi(\vec{x} - \vec{r}, t)\mathrm{d}\vec{r}, \tag{2.19}$$

where the $\widetilde{\varphi}$ is a filtered variable, G is the normalized filter function and $\vec{r}$ is a position vector [34]. The filtered variable is defined as $\widetilde{\varphi} = \varphi - \varphi'$. It can be used to filter the variables in Eq. (2.14). After applying the filter to pressure and velocity in Eq. (2.14), including gravitational and Coriolis force and using the Boussinesq approximation for the density variations, Navier-Stokes equation can be written as

$$\begin{aligned}\underbrace{\frac{\partial \widetilde{u}_i}{\partial t}}_{\text{storage}} = &- \underbrace{\widetilde{u}_j \frac{\partial \widetilde{u}_i}{\partial x_j}}_{\text{advection}} - \underbrace{c_p \Theta_0 \frac{\partial \widetilde{\pi}}{\partial x_i}}_{\text{pressure-gradient}} + \underbrace{\frac{g\widetilde{\theta}''_v}{\theta_0}}_{\text{gravity}} \delta_{i3} + \underbrace{f_k(\widetilde{u}_j - u_{j,g})\epsilon_{ijk}}_{\text{Coriolis}} \\ &+ \underbrace{\frac{1}{\rho_0}\frac{\partial(\rho_0\,\tau_{ij})}{\partial x_j}}_{\text{viscous stress}}\end{aligned} \tag{2.20}$$

where $f_k = \{0, 0, 2\,\Omega \sin\phi\}$ is the Coriolis parameter, $u_{j,g}$ is the geostrophic wind, $\tau_{ij} = \widetilde{u_i u_j} - \widetilde{u}_i\widetilde{u}_j$ is the sub-filter scale stress tensor, $\theta_0$ is the basic state potential temperature and $\widetilde{\theta}''_v$ is the deviation of $\widetilde{\theta}_v$ from its horizontal average ensuring that there is no vertical acceleration [35]. Using the same method, Eq. (2.18) can be written as

$$\frac{\partial \widetilde{\varphi}}{\partial t} = -\widetilde{u}_j \frac{\partial \widetilde{\varphi}}{\partial x_j} + \frac{1}{\rho_0}\frac{\partial(\rho_0 \gamma_{\varphi j})}{\partial x_j} + \frac{\partial S_\varphi}{\partial x_j}\delta_{j3}, \tag{2.21}$$

where $\rho_0$ is the air density and $\gamma_{\varphi j} = \widetilde{\varphi u_j} - \widetilde{\varphi}\widetilde{u}_j$ is the sub-filter scale flux. Usually in the boundary layer air can be considered incompressible, thus Eq. (2.12) can be written as

$$\frac{\partial \rho_0 u_i}{\partial x_i} = 0 \tag{2.22}$$

which is the anelastic approximation.

To derive the pressure equation, divergence ($\frac{\partial}{\partial x_i}$) of Eq. (2.20) is taken which equals to zero according to the continuity Eq. (2.22). This yields to

$$\begin{aligned}\frac{\partial}{\partial x_i}\left(\rho_0 \frac{\widetilde{u}_i}{\partial t}\right) = \frac{\partial}{\partial x_i}\Bigg[&-\rho_0 \widetilde{u}_j \frac{\partial \widetilde{u}_i}{\partial x_j} - \rho_0 c_p \Theta_0 \frac{\partial \widetilde{\pi}}{\partial x_i} + \frac{\rho_0 g \widetilde{\theta}''_v}{\theta_0}\delta_{i3} \\ &+\rho_0 f_k(\widetilde{u}_j - u_{j,g})\epsilon_{ijk} + \frac{\partial(\rho_0 \tau_{ij})}{\partial x_j}\Bigg] = 0,\end{aligned} \tag{2.23}$$

rearranging the equation, we get

$$\frac{\partial}{\partial x_i}\left(\rho_0 c_p \Theta_0 \frac{\partial \widetilde{\pi}}{\partial x_i}\right) = \frac{\partial}{\partial x_i}\left[-\rho_0 \widetilde{u}_j \frac{\partial \widetilde{u}_i}{\partial x_j} + \frac{\rho_0 g \widetilde{\theta}_v''}{\theta_0}\delta_{i3} \right.$$
$$\left. + \rho_0 f_k(\widetilde{u}_j - u_{j,g})\epsilon_{ijk} + \frac{\partial(\rho_0 \tau_{ij})}{\partial x_j}\right]. \tag{2.24}$$

Finally the constants are shifted to the right hand side and the Poisson equation for the pressure is

$$\frac{\partial}{\partial x_i}\left(\rho_0 \frac{\partial \widetilde{\pi}}{\partial x_i}\right) = \frac{1}{c_p \Theta_0}\left[\frac{\partial}{\partial x_i}\left(-\rho_0 \widetilde{u}_j \frac{\partial \widetilde{u}_i}{\partial x_j} + \frac{\rho_0 g \widetilde{\theta}_v''}{\theta_0}\delta_{i3} \right.\right.$$
$$\left.\left. + \rho_0 f_k(\widetilde{u}_j - u_{jg})\epsilon_{ijk} + \frac{\partial(\rho_0\, \tau_{ij})}{\partial x_j}\right)\right]. \tag{2.25}$$

The sub-grid fluxes $\tau_{ij}$ and $\gamma_{\phi j}$ in Eq. (2.20) and Eq. (2.21) are not known explicitly and thus they have to be modeled. In UCLA LES this is done using the Smagorinsky model where $\tau_{ij}$ is defined as

$$\tau_{ij} = -\rho_0 K_m \left(\frac{\partial \widetilde{u}_i}{\partial x_j} + \frac{\partial \widetilde{u}_j}{\partial x_i}\right) = -\rho_0 K_m D_{ij} \tag{2.26}$$

and $\gamma_{\phi j}$ is

$$\gamma_{\phi j} = -\frac{K_m}{Pr}\frac{\partial \widetilde{\phi}}{\partial x_j}, \tag{2.27}$$

where $D_{ij}$ is the resolved deformation, $Pr$ is the eddy Prandtl number and $K_m$ is the eddy viscosity [36]. Prandtl number is a dimensionless number which is the ratio of momentum diffusivity to thermal diffusivity. Its value is set to 0.3 in UCLA LES [37]. To calculate the eddy viscosity $K_m$ we first define local sub-grid scale Richardson number

$$Ri = \frac{S^2}{N^2} \tag{2.28}$$

where the magnitude of deformation $S$ and Brunt-Väisälä frequency $N$ is defined as

$$S^2 = \frac{\partial \widetilde{u}_j}{\partial x_i}\left(\frac{\partial \widetilde{u}_i}{\partial x_j}\frac{\partial \widetilde{u}_i}{\partial x_j}\right) \quad \text{and} \quad N^2 = \frac{g}{\Theta_0}\frac{\partial \widetilde{\theta}_v}{\partial z}. \tag{2.29}$$

Then we can write $K_m$ as

$$K_m = (C_s \ell)^2 S \sqrt{1 - \frac{Ri}{Pr}} \tag{2.30}$$

where $C_s$ is the Smagorinsky with a value of 0.2 and $\ell$ is the length scale defined as

$$\ell^{-2} = (\Delta x \Delta y \Delta z)^{-2/3} + (z\kappa/C_s)^{-2}, \tag{2.31}$$

where $\kappa$ is the von Kármán constant and is set to 0.35.

## 2.4 UCLA LES model

The UCLA LES model is programmed using FORTRAN90 [38]. The structure of the code is highly modular which means that it consists of modules, which in turn consist of subroutines. One module usually deals with one larger task. For example, the microphysics module includes all the subroutines for microphysical processes. The stepper module has the main loop of the program which will call all the relevant subroutines during each time step. The initial values for a simulation are controlled from a single namelist file. During the model execution it writes out the time-averaged field values to 3 different NetCDF[1] files. The model can be either run using one processor or using multiple processors. It is parallelized by decomposing the domain into sub-domains consisting of columns in the horizontal plane and using a MPI library. To make it easier to read the model code the variable names used in the thermodynamic module are listed in Table 5 and the variable names used in the microphysical module are listed in Table 6 in Appendix A.

Here a short summary all the parts of the model is represented. The model can be roughly divided to three different parts: dynamics, radiation and cloud microphysics. The dynamics used in the model can be summarized as follows

- Boussinesq approximation is assumed for Navier-Stokes equation and LES-filter is applied to the equations.
- Turbulence closure uses the Smagorinsky model.
- The Arakawa-C grid is doubly periodic in horizontal direction and bounded in the vertical direction. The horizontal grid is uniform and vertical grid is stretchable.

[1] NetCDF library. `http://www.unidata.ucar.edu/software/netcdf/`

- In top of the domain a sponge layer dampens the motion mimicking the free atmosphere.
- Scalar terms are time-stepped using a forward scheme staggered with respect to the time-levels of the momentum terms, so that the advecting winds correspond to the mid-point times. Scalar advection is Total Variation Diminishing (TVD)[2] and uses the Monotonized Central (MC) flux-limiters[39].
- Momentum advection uses directionally split fourth-order centered differences. The vertical advection is density weighted consistent with the anelastic approximation.
- The Poisson equation for the modified pressure $\pi$ is solved with a Fast Fourier transform in the horizontal direction. For vertical direction a tridiagonal system is solved.

The radiative routines in the model can summarized as follows

- Radiation scheme is based on the Fu & Liou scheme where delta-four-stream method is used to solve the azimuth-averaged radiative transfer equation [40].
- To calculate the spectral transmittances, a correlated k-distribution method is used. It groups gaseous spectral transmittances according to the absorption coefficient $k_\nu$ and transforms the renumber integration to integration over k-space [41].
- Radiative properties of ice crystals are parametrized using third-order polynomials [42].

Finally, the cloud microphysical and thermodynamics of the model are as follows

- Time-stepping is based on the third order Runge-Kutta method.
- Cloud water microphysics is a hybrid one-moment bulk parametrization where number concentration of CCN is a constant.
- Parametrization of rain and cloud water microphysics is based on Seifert and Beheng model [43]. Exponential distribution is assumed and the

[2]The use of higher order scheme can induce spurious oscillation which are dampened using flux-limiters. This guarantees that the solution is Total Variation Diminishing (TVD).

processes include evaporation in the absence of cloud water, autoconversion[3], accretion[4], self-collection[5] and sedimentation.

- Cloud ice mixing ratio and cloud ice number mixing ratio follow parts of the Seifert and Beheng model.
- Ice particle are assumed to be hexagonal plates evolving according to generalized Γ-distribution.
- Ice microphysical processes are nucleation of ice, freezing of cloud and rain water, growth of ice by water vapor deposition and sedimentation.

[3] Formation of rain droplets by coagulating cloud droplets.
[4] Growth of rain droplets collecting cloud droplets.
[5] Mutual coagulation of a same droplet category.

# 3 Ice microphysics

The so called Kessler scheme is one of the first, and is still used today parametrization approaches to the cloud microphysics [44]. This approach was originally formulated for warm clouds, and with the method clouds are modeled considering their mass densities only. The liquid water is partitioned to cloud water and rain water. Within this scheme, Kessler introduced the term autoconversion meaning conversion from cloud droplets to rain droplets and accretion meaning growth of rain droplets by collecting cloud droplets. This kind of bulk parametrization of cloud microphysical processes has a long standing tradition in modeling the cloud microphysics. Using this idea, an ice cloud microphysical scheme was constructed by Rutledge and Hobbs [45]. In addition to water vapor, cloud water, and rain, this parametrization introduced categories for ice, snow, graupel and hail. It is important to note that these parametrizations did not explicitly calculate the number densities of each droplet category. Since then, almost complete two-moment bulk parametrizations, that consider the number density of all ice cloud categories, have been developed [46][47][48].

The Seifert and Beheng (SB) model is a parametric distribution method which has rate equations for all the five hydrometeor types including the prediction of Cloud Condensation Nuclei (CCN) number concentration [43]. It is assumed that the particles are continuously distributed over their size range which means that one hydrometeor type can be described by its number and mass distributions instead of explicitly modeling each individual particle. Furthermore, a certain shape of distribution is also assumed. For example in the UCLALES model the distribution of rain mass mixing ratio is assumed to be an exponential distribution. This way the distribution can be solved using the mean size, standard deviation of sizes and the total number of particles.

The SB model in its full form is a very complicated microphysical scheme and for the purpose of this study only part of it was implemented. In Figure 3 there is a schematic of the microphysics of the UCLA LES model that was used. On the left side of the figure are the warm cloud processes which start when cloud water forms in saturated conditions. After that, droplets continue to grow due to collisions, and eventually rain is developed when cloud droplet radius is higher than 80 µm.

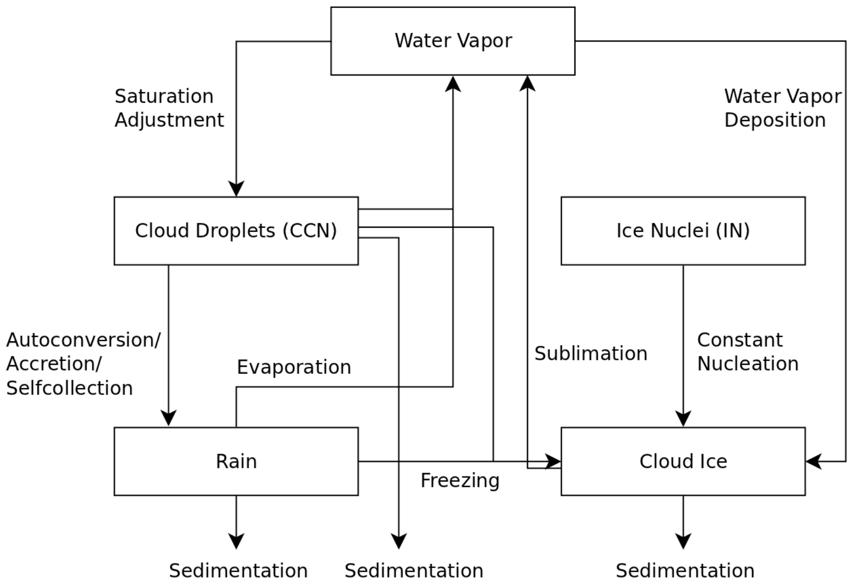


Figure 3: Cloud microphysics of the UCLA LES model.

Ice starts to develop when the ice nucleation happens in suitable conditions and ice nuclei (IN) form. From these particles ice crystals can form and grow mainly due to water vapor deposition. Ice crystals can also form by freezing of cloud and rain droplets. For all these particles, sedimentation is included, and it will make them eventually settle on the surface.

In this chapter, the general gamma distribution is revised and the microphysical parametrizations for nucleation, freezing of cloud/rain droplets, water vapor deposition and sedimentation of ice are presented. In the end there is a summary of the equations covering the scalar variables.

## 3.1 Generalized Γ-distribution

One of the most common cloud drop and raindrop number distribution function used in the cloud microphysical parametrizations is the Γ-distribution. It is defined as

$$f(x) = Ax^{\nu}\exp(-\lambda_{sb}x^{\mu_{sb}}), \tag{3.1}$$

where x is the the particle mass and $\mu_{sb}$, $\nu$, $\lambda_{sb}$ and A are shape parameters [43]. The parameters A and $\lambda_{sb}$ can be expressed by the number and mass densities as

$$A = \frac{\mu_{sb} N}{\Gamma\left(\frac{\nu+1}{\mu_{sb}}\right)} \lambda_{sb}^{\frac{\nu+1}{\mu_{sb}}} \text{ and } \lambda_{sb} = \left[\frac{\Gamma\left(\frac{\nu+1}{\mu_{sb}}\right)}{\Gamma\left(\frac{\nu+2}{\mu_{sb}}\right)} \bar{x}\right]^{-\mu_{sb}} \tag{3.2}$$

where $\bar{x} = \frac{r'}{N'}$ is the mean particle mass, $r'$ is the mass density of a droplet and $N'$ is the number density of droplets. The prime is used to distinguish number and mass densities from the mixing ratios. By substituting Eq. (3.2) to Eq. (3.1), the generalized $\Gamma$-distribution can be written as a function of number and mass densities in the form

$$f(x) = \frac{N'}{\bar{x}} \left[\frac{x}{\bar{x}}\right]^{\nu} \frac{\mu_{sb}}{\Gamma\left(\frac{\nu+1}{\mu_{sb}}\right)} \left[\frac{\Gamma\left(\frac{\nu+2}{\mu_{sb}}\right)}{\Gamma\left(\frac{\nu+1}{\mu_{sb}}\right)}\right]^{\nu+1} \times \exp\left\{-\left[\frac{\Gamma\left(\frac{\nu+2}{\mu_{sb}}\right)}{\Gamma\left(\frac{\nu+1}{\mu_{sb}}\right)} \frac{x}{\bar{x}}\right]^{\mu_{sb}}\right\} \tag{3.3}$$

The nth power moment is given by

$$M^n = \frac{\Gamma\left(\frac{n+\nu+1}{\mu_{sb}}\right)}{\Gamma\left(\frac{\nu+1}{\mu_{sb}}\right)} \left[\frac{\Gamma\left(\frac{\nu+1}{\mu_{sb}}\right)}{\Gamma\left(\frac{\nu+2}{\mu_{sb}}\right)}\right]^{n} N' \bar{x}^n \tag{3.4}$$

For ice crystal population the zeroth moment of the $f(x)$ is the number density of ice crystals $M^0 = N_i'$ and the first moment is the mass density of ice crystals $M^1 = r_i'$.

## 3.2 Ice nucleation

The process of ice nucleation is substantially more complicated than the formation of droplets. While CCN are sensitive primarily to the supersaturation with respect to water, the activity of IN depends on supersaturation and temperature. The nuclei are small aerosols varying in size from 0.01 µm to 10 µm. The ice nucleation by IN is called heterogeneous ice nucleation as it involves a foreign substance on which ice water can form. There are at least four distinct heterogeneous ice nucleation modes (or mechanisms) through which IN may form ice particles, compared to the one process of activation of CCN. According to Khain et al. [49] these modes are

- Deposition nucleation, when water vapor is absorbed directly onto the surface of nucleus where it transforms into ice.
- Condensation–freezing nucleation, which is a sequence of events when, first a film of liquid is formed on the surface of the nucleus, and then the condensate freezes.
- Immersion–freezing nucleation, when freezing of droplets is induced by nuclei located within the droplets themselves.
- Contact nucleation, when freezing of the droplet is caused by the contact of supercooled drops and nucleus.

In addition, Hallet and Mossop postulated a secondary ice nucleation method in which the freezing of supercooled water to graupel ejects numerous small ice nuclei [50] [51].

In the SB model heterogeneous ice nucleation is based on the experimental formula by Meyer [52]. It combines the effects of deposition-condensation freezing and contact nucleation. The data used to derive the equations is obtained from continuous flow diffusion chambers. The deposition-condensation freezing is defined as

$$N_{id} = \exp(-0.639 + 0.1296(100(S_i - 1))) \tag{3.5}$$

where $S_i$ is the supersaturation with respect to ice. This equation was strictly developed from data between temperatures of -7 to -20 ℃ and between ice saturation from 2% to 25% or from -5 to +4.5% with respect to liquid water. The contact nucleation is defined as

$$N_{ic} = \exp(-2.8 + 0.262(273.15 - T_{cd})) \tag{3.6}$$

where $T_{cd}$ is the cloud droplet temperature. The values of depositional-condensational freezing and contact nucleation are summed to get the total ice nuclei number concentration

$$N_{IN} = N_{id} + N_{ic}. \tag{3.7}$$

Following the mechanism introduced by Reisner et al. [48] and followed by Seifert and Beheng [43] the ice nucleation rate is calculated as follows

$$\frac{\partial N_{IN}}{\partial t} = \begin{cases} \dfrac{N_{IN}(S_i, T) - N_{Tii}}{\Delta t}, & \text{if } S_i \geq 0 \text{ and } N_{Tii} < N_{Ti}(S_i, T) \\ 0, \ \text{otherwise,} & \end{cases} \tag{3.8}$$

where $N_{Tii}$ is the initial ice nuclei concentration.

## 3.3 Freezing of cloud and rain drops

Experiments with water drops containing various impurities have revealed that their freezing temperature is a function of the drop volume. Bigg suggested that at a given temperature all equal-sized ice nuclei formed in a population of equal-sized supercooled water drops have an equal probability of reaching the size of a critical ice nuclei as a result of random fluctuations among the water molecules [53]. This is the classical stochastic hypothesis of freezing. Also the laboratory experiments suggest that drop freezing is likely a stochastic process and that it is a function of the volume of the liquid-water particle and the number of ice nuclei that can activate in drops at a given temperature [54].

Assuming the classical stochastic hypothesis, the relative time rate of change of the cloud droplet size distribution by heterogeneous freezing is given by

$$\frac{1}{f_c(x)}\frac{\partial f_c(x)}{\partial t} = -x\,A_{het}\,\exp[B_{het}(T-273.15)-1] = -x\,J_{het}(T) \tag{3.9}$$

where $f_c(x)$ is the size distribution, $A_{het} = 0.2$ and $B_{het} = 0.65$ [49]. The corresponding moment equation is then given by

$$\frac{\partial M_c^{k+1}}{\partial t} = -M_c^{k+1} J_{het}(T) \tag{3.10}$$

To close the equations, (3.9) and (3.10), a $\Gamma$-distribution is assumed for $f_c(D)$, which results to

$$\frac{\partial r_c}{\partial t} = -\frac{\Gamma\left(\frac{2+\nu+1}{\mu_{sb}}\right)}{\Gamma\left(\frac{\nu+1}{\mu_{sb}}\right)}\left[\frac{\Gamma\left(\frac{\nu+1}{\mu_{sb}}\right)}{\Gamma\left(\frac{\nu+2}{\mu_{sb}}\right)}\right]^2 \bar{x}_c J_{het}(T), \tag{3.11}$$

where mixing ratio is used instead of the moment of distribution. The mean mass of cloud droplet $\bar{x}_c$ is defined as

$$\bar{x}_c = \min(\max(\frac{r_c}{n_{CCN}}, r_{c,min}), r_{c,max}) \tag{3.12}$$

The corresponding addition to the cloud ice mass is

$$\left.\frac{\partial r_i}{\partial t}\right|_{frz} = \frac{\Gamma\left(\frac{2+\nu+1}{\mu_{sb}}\right)}{\Gamma\left(\frac{\nu+1}{\mu_{sb}}\right)}\left[\frac{\Gamma\left(\frac{\nu+1}{\mu_{sb}}\right)}{\Gamma\left(\frac{\nu+2}{\mu_{sb}}\right)}\right]^2 \bar{x}_c J_{het}(T). \tag{3.13}$$

Similar addition without the mean mass $\bar{x}_c$ is added to the ice crystal number concentration. This freezing happens when the absolute temperature $T \leq 273.15$ K and cloud water is present. The freezing of rain water was done similarly but assuming an exponential size distribution.

## 3.4 Water vapor deposition to ice

The ice crystal can grow by vapor deposition if the environment is supersaturated with respect to ice. The saturation vapor pressure with respect to ice is less than the saturation vapor pressure with respect to water at the same temperature. This means that a cloud which is saturated with respect to water will have a higher supersaturation with respect to ice. This leads to the Bergeron-Findeisen process in which liquid water is evaporating and ice crystals are growing by vapor deposition [55].

Depositional growth of a single ice particle can be described using the general growth equation as follows

$$\frac{dx_i}{dt} = \frac{4\pi C_i F_v(x_i) S_i}{\frac{R_v T}{p_{iv}(T) D_v} + \frac{L_{iv}}{K_T T}\left(\frac{L_{iv}}{R_v T} - 1\right)} = \frac{4\pi}{c_i} D_i G_{iv}(T,p) F_v(x_i) S_i, \tag{3.14}$$

where $x_i$ is the mass of an ice particle, $C_i$ is the capacitance of spherical particle, $F_v$ is the ventilation coefficient, $S_i$ is the supersaturation with respect to ice, $R_v$ is the gas constant for water vapor, $D_v$ is the diffusivity of water vapor, $K_T$ is the conductivity of heat, $D_i$ is the diameter of the particle, $L_{iv}$ is the latent heat of sublimation and $p_{iv}(T)$ is the saturation vapor pressure over ice [56]. For hexagonal plate $c_i$ is equal to $\pi$. The $G_{iv}$ is defined as

$$G_{iv}(T,p) = \left[\frac{R_v T}{p_{iv}(T) D_v} + \frac{L_{iv}}{K_T T}\left(\frac{L_{iv}}{R_v T} - 1\right)\right]^{-1} \tag{3.15}$$

and the saturation vapor pressure over ice is defined as

$$p_{iv}(T) = 6.1078 \exp\left(21.8745584 \frac{T - 273.16}{T - 7.66}\right), \tag{3.16}$$

where temperature is in Kelvin and $p_{iv}$ is in hPa [57]. The diameter of the particle is expressed using the diameter-mass

$$D_i(x) \cong a_i\, x_i^{b_i}, \tag{3.17}$$

where $a_i = 0.217$ and $b_i = 0.302$ [58]. Integration of Eq. (3.14) results in an equation for the mass density of a particle ensemble

$$\frac{\partial r_i'}{\partial t} = 4\, G_{iv}(T,p) S_i \int_0^\infty D_i(x) F_v(x) f_i(x) \mathrm{d}x. \tag{3.18}$$

Assuming generalized $\Gamma$-distribution for $f_i(x)$ and integrating Eq. (3.18) we get equation for the mixing ratio

$$\left.\frac{\partial r_i}{\partial t}\right|_{dep} = 4\, G_{iv}(T,p) D_i(\bar{x}) \bar{F}_v S_i N_i, \tag{3.19}$$

where $N_i$ is the ice crystal number concentration. The average ventilation coefficient is given by

$$\bar{F}_v = \bar{a}_{vent} + \bar{b}_{vent} N_{Sc}^{\frac{1}{3}} N_{Re}^{\frac{1}{2}}(\bar{x}_i). \tag{3.20}$$

with the Schmidt number $N_{Sc} = 0.71$ and the Reynolds number $N_{Re}$. The constants $\bar{a}_{vent}$ and $\bar{b}_{vent}$ are given by

$$\bar{a}_{vent} = a_v \frac{\Gamma\left(\frac{\nu+b_i+1}{\mu_{sb}}\right)}{\Gamma\left(\frac{\nu+1}{\mu_{sb}}\right)} \left[\frac{\Gamma\left(\frac{\nu+1}{\mu_{sb}}\right)}{\Gamma\left(\frac{\nu+2}{\mu_{sb}}\right)}\right]^{b_i} \tag{3.21a}$$

$$\bar{b}_{vent} = b_v \frac{\Gamma\left(\frac{\nu+\frac{3}{2}b_i+\frac{1}{2}\beta_i+1}{\mu_{sb}}\right)}{\Gamma\left(\frac{\nu+1}{\mu_{sb}}\right)} \left[\frac{\Gamma\left(\frac{\nu+1}{\mu_{sb}}\right)}{\Gamma\left(\frac{\nu+2}{\mu_{sb}}\right)}\right]^{\frac{3}{2}b_i+\frac{1}{2}\beta_i} \tag{3.21b}$$

with the coefficients $\alpha_i$ and $\beta_i$ from the velocity-mass relation

$$v_i(x) \cong \alpha_i x_i^{\beta_i}. \tag{3.22}$$

where $\alpha_i = 317$ and $\beta_i = 0.363$. The average Reynolds number of a single ice particle falling with terminal fall velocity $v_i$ is

$$N_{Re}(\bar{x}) = \frac{v_i D_i(\bar{x})}{\nu_{air}} \tag{3.23}$$

where $\nu_{air}$ is the kinematic viscosity of air and the mean mass of ice crystals is defined as

$$\bar{x}_i = \min(\max(\frac{r_i}{N_i}, r_{i,min}), r_{i,max}) \tag{3.24}$$

where $r_{i,min} = 1 \times 10^{-12}$ kg is the minimum mass and $r_{i,max} = 7 \times 10^{-12}$ kg is the maximum mass of ice crystal.

## 3.5 Sedimentation

Sedimentation of rain drops in UCLA LES is in accordance with the Seifert and Beheng model [59]. For rain drops exponential distribution is assumed and is calculated as in their article. First, the sedimentation velocities are calculated and then sedimentation fluxes are calculated using the upwind Eulerian scheme for both mass and number mixing ratios. However, only the sedimentation flux of mass mixing ratio affects to the evolution of $r_t$ and $\theta_l$. Sedimentation of cloud drops is calculated assuming a log-normal distribution and is based on mass-weighted mean fall velocities [60]. The cloud drop sedimentation only affects the evolution of $r_t$ and $\theta_l$.

The sedimentation of the ice particles follows the same approach as the rain droplet sedimentation. By assuming the velocity-mass relation of Eq. (3.22) and generalized Γ-distribution for $f_i(x)$ we get the mean fall velocities for the k-th moment of ice crystals as follows

$$\bar{v}_{i,k}(\bar{x}) = \alpha_i \frac{\Gamma\left(\frac{k+\nu+\beta_i+1}{\mu_{sb}}\right)}{\Gamma\left(\frac{k+\nu+1}{\mu_{sb}}\right)} \left[\frac{\Gamma\left(\frac{\nu+1}{\mu_{sb}}\right)}{\Gamma\left(\frac{\nu+2}{\mu_{sb}}\right)}\right]^{\beta_i} \bar{x}_i^{\beta_i} \tag{3.25}$$

where $k = 0$ for the number concentration and $k = 1$ for the mass mixing ratio. The sedimentation fluxes for $N_i$ and $r_i$ are calculated using the flux-form semi-Lagrangian scheme with the mean fall velocities $\bar{v}_{i,0}$ and $\bar{v}_{i,1}$ . The details of the semi-Lagrangian approach is given by Stevens et al. [61].

## 3.6 Summary

In this chapter all the sink and source terms affecting the ice clouds are collected into the scalar advection equations. The prognostic equation for $r_i$

in vector form is

$$\frac{\partial r_i}{\partial t} = -\vec{u} \cdot \nabla r_i + \nabla \cdot (K_h \nabla r_i) - \bar{v}_{i,1} \frac{\partial r_i}{\partial z} + \left.\frac{\partial r_i}{\partial t}\right|_{nuc} + \left.\frac{\partial r_i}{\partial t}\right|_{frz} + \left.\frac{\partial r_i}{\partial t}\right|_{dep}, \tag{3.26}$$

where $K_h$ is the eddy diffusivity of heat and it is defined as $K_h = \frac{K_m}{Pr}$. Similarly for the ice crystal number concentration we get

$$\frac{\partial N_i}{\partial t} = -\vec{u} \cdot \nabla N_i + \nabla \cdot (K_h \nabla N_i) - \bar{v}_{i,0} \frac{\partial N_i}{\partial z} + \left.\frac{\partial N_i}{\partial t}\right|_{nuc} + \left.\frac{\partial N_i}{\partial t}\right|_{frz} + \left.\frac{\partial N_i}{\partial t}\right|_{dep} \tag{3.27}$$

Occasionally, due to the leap-frog advection scheme the microphysical variables in Eqs. (3.26)–(3.27) can become negative. To circumvent this problem the negative values were set to zero.

Sedimentation and scalar advection schemes both use flux limiters to ensure that they can not produce unrealistic concentrations. Still, the sum of these individual terms can produce negative values. For this reason, during each time step negative values of number and mass concentrations were adjusted to be zero. In addition, the masses of all kind of particle types were adjusted between the defined maximum and minimum values to avoid artificial growth.

# 4 Radiation

In this chapter general radiative transfer equation and the numerical method used in the UCLA LES model to solve it, are presented. To make efficient radiative calculations in LES models, a full 3-dimensional form of the radiative transfer equation cannot be used. Instead, the atmosphere is divided into vertical levels which are in local thermodynamic equilibrium which enables to use the azimuth-averaged equation. This equation is discretized and solved using numerical methods. Also, the ice crystal parametrization and the Monte Carlo spectral method for radiative transfer are presented.

## 4.1 Atmospheric radiative transfer

Radiation traversing a medium will be weakened by its interaction with matter. If the intensity $I_\lambda$ becomes $I_\lambda + dI_\lambda$ after traversing a thickness ds in the direction of its propagation, then

$$\mathrm{d}I_\lambda = -k_\lambda \rho I_\lambda \mathrm{d}s, \tag{4.1}$$

where $\rho$ is the density of the material, $k_\lambda$ denotes the mass extinction (sum of mass absorption and scattering) cross section for radiation of wavelength $\lambda$ [26]. Thus, the reduction is due to absorption by the material as well as to scattering by the material. On the other hand, the intensity can increase due to emission from the material or to multiple scattering from all other directions. We can define the increase as

$$\mathrm{d}I_\lambda = j_\lambda \rho \mathrm{d}s \tag{4.2}$$

where $j_\lambda$ is the coefficient for emission and multiple scattering. Now we can write the general radiative heat transfer equation as

$$\mathrm{d}I_\lambda = -k_\lambda \rho I_\lambda \mathrm{d}s + j_\lambda \rho \mathrm{d}s, \tag{4.3}$$

which is usually written in the form

$$\frac{\mathrm{d}I_\lambda}{k_\lambda \rho \mathrm{d}s} = -I_\lambda + J_\lambda, \tag{4.4}$$

where $J_\lambda = \frac{j_\lambda}{k_\lambda}$. This is the base of all radiative transfer calculations which can be solved with certain assumptions and approximations depending on the case.

In the following section only thermal infrared radiation is considered when solving Eq. (4.4). Usually when modeling radiative transfer, the thermal infrared and solar radiations are solved separately in the models. For solar radiation the derivation is the same with a different source term $J_\lambda$ in Eq. (4.4).

For an absorbing and emitting medium the equation Eq. (4.4) can be written as

$$-\frac{1}{k_\lambda \rho_a}\frac{\mathrm{d}I_\lambda}{\mathrm{d}s} = I_\lambda - J_\lambda \tag{4.5}$$

where $k_\lambda$ denotes the absorption coefficient, $\rho_a$ is the density of absorbing gases, $s$ is the slant path and $J_\lambda$ is the source function. Atmosphere is usually considered to be in local thermodynamic equilibrium which enables to use Planck intensity for the source function $J_\lambda$. It is also assumed that the variations in intensity $I_\lambda$ and in thermodynamic variables are permitted only in the vertical direction. This is the azimuth-averaging assumption which enables to write intensity as a function of zenith angle and vertical position. Under these assumptions Eq. (4.5) can be written as

$$-\mu\frac{\mathrm{d}I_\lambda(z,\mu)}{k_\lambda \rho_a \mathrm{d}z} = I_\lambda(z,\mu) - B_\lambda(z), \tag{4.6}$$

where $B_\lambda(z)$ is the Planck intensity and $\mu = \cos\theta$ is the zenith angle.

In thermal infrared radiation within clouds, scattering takes place and the Eq. (4.6) has to be modified to account for scattering processes. This leads to equation

$$\mu\frac{\mathrm{d}I_\lambda}{\mathrm{d}z} = -\beta_a(I_\lambda - B_\lambda) - \beta_s(I_\lambda - J_\lambda) = -\beta_e(I_\lambda - S_\lambda), \tag{4.7}$$

where the extinction coefficient is $\beta_e = \beta_s + \beta_a$ (index s stands for scattering and index a stands for absorption) and source function $S_\lambda = (\beta_a B_\lambda + \beta_s J_\lambda)/\beta_e$.

A single scattering albedo can now be defined as $\tilde{\omega}_\lambda = \beta_s/\beta_e$. It is a very important variable in radiation which for value of unity implies that all particle extinction is due to scattering and conversely, zero implies that all extinction is due to absorption. Also, the dependence in vertical direction can be changed to depend on the optical depth which is defined as

$$\tau = \int_z^\infty \beta_e \mathrm{d}z'. \tag{4.8}$$

Noting that $\mathrm{d}\tau = -\beta_e \mathrm{d}z$ and the source function $S_\lambda = (1-\tilde{\omega}_\lambda)B_\lambda + \tilde{\omega}_\lambda J_\lambda$ we can write Eq. (4.7) as

$$\mu \frac{\mathrm{d}I_\lambda}{\mathrm{d}\tau} = I_\lambda - \tilde{\omega}_\lambda J_\lambda - (1-\tilde{\omega}_\lambda)B_\lambda, \tag{4.9}$$

For the source function of scattering, only azimuth-independent component is considered:

$$J_\lambda = \frac{1}{2}\int_{-1}^{1} I_\lambda(\tau,\mu')P(\mu,\mu')\mathrm{d}\mu', \tag{4.10}$$

where the phase function $P$ represents the angular distribution of the scattered energy as a function of the scattering angle and is defined as

$$P(\mu,\mu') = \frac{1}{2\pi}\int_0^{2\pi} P(\cos\Theta)\mathrm{d}\phi', \tag{4.11}$$

where the cosine of the scattering angle is defined by $\cos\Theta = \mu\mu' + (1-\mu^2)^{\frac{1}{2}}(1-\mu'^2)^{\frac{1}{2}}\cos\phi$, with $\phi$ the azimuthal angle and $\mu'$ is the multiple scattering angle. Combining Eq. (4.9) and Eq. (4.10), and leaving out the $\lambda$ in the index of the variables, we get the azimuth-averaged equation governing the transfer of diffuse infrared intensity $I$ in plane-parallel atmospheres and local thermodynamic equilibrium

$$\mu\frac{\mathrm{d}I(\tau,\mu)}{\mathrm{d}\tau} = I(\tau,\mu) - \frac{\tilde{\omega}}{2}\int_{-1}^{1} I(\tau,\mu')P(\mu,\mu')\mathrm{d}\mu' - (1-\tilde{\omega})B(T), \tag{4.12}$$

where $\mu = \cos(\theta)$ is the zenith angle, $\tau$ the normal optical depth, $\tilde{\omega}$ single-scatter albedo and $B(T)$ the black-body intensity at temperature T.

Solving Eq. (4.12) for the absorbing gases ($H_2O$, $CO_2$, $CH_4$, $N_2O$ and $O_3$), is computationally demanding because these gases have large number of spectral lines which requires very small increments of wave number in the spectral integration. In UCLA LES model calculation of the spectral transmittance uses a correlated k-distribution method which groups gaseous spectral transmittances according to the absorption coefficient $k_\lambda$ and transform the number integration to integration over k-space [41].

## 4.2 Discrete radiative transfer equation

To be able to solve Eq. (4.12) numerically it has to discretized. First, the scattering phase function can be expanded using Legendre polynomials as follows

$$P(\cos\Theta) = \sum_{l=0}^{N} \tilde{\omega}_l P_l(\cos\Theta), \tag{4.13}$$

where $P_l$ is the Legendre polynomial [62]. Then, the additional theorem of Legendre polynomials can be used to write the the azimuth-independent phase function as follows

$$P(\mu, \mu') = \sum_{l=0}^{N} \tilde{\omega}_l P_l(\mu) P_l(\mu'). \tag{4.14}$$

By replacing the integrations in the Eq. (4.12) by summation using the Gauss quadrature and phase function using Eq. (4.14) leads to

$$\begin{aligned} \mu_i \frac{\mathrm{d}I(\tau, \mu_i)}{\mathrm{d}\tau} &= I(\tau, \mu_i) - \frac{\tilde{\omega}}{2} \sum_{t=0}^{N} \tilde{\omega}_l P_l(\mu_i) \times \sum_{j=-n}^{n} I(\tau, \mu_j) P_l(\mu_j) a_j \\ &\quad - (1 - \tilde{\omega}) B(T), \end{aligned} \tag{4.15}$$

where $i = \pm 1, ..., \pm n$, quadrature point $\mu_{-j} = -\mu_j$, $j \neq 0$ and the weight $a_{-j} = a_j$ and $\sum_{j=-n}^{n} a_j = 2$ [40]. The upward and downward fluxes at a given level $\tau$ are then defined by

$$F^{\pm}(\tau) = 2\pi \sum_{i=1}^{n} a_i \mu_i I(\tau, \pm\mu_i). \tag{4.16}$$

where $F^+$ is the upward flux and $F^-$ is the downward flux. In UCLA LES model numerical approximation called Delta-four-stream method is used to solve Eqs. (4.15) and (4.16) [40].

## 4.3 Ice crystal parametrization

In this study a simple parametrization of broadband solar and infrared radiative properties of ice clouds based on the Fu & Liou scheme was added to the UCLA LES model [42]. The addition of the ice parametrization was easy because the optical properties in the model are calculated using an additive method and the broadband division into 6 bands for solar and 12 bands for thermal infrared radiation, is the same as in the UCLA LES model. The ice crystals are represented by parametrizing the key quantities using a third-degree polynomials which are fitted to observed values obtained from in situ aircraft observations for different clouds. Here, only equations are presented and the coefficient tables can be found in the original paper [42].

Two important variables are used to define optical properties of the ice clouds. The first one being the ice crystal size which is expressed in terms of the maximum dimension. We can define the mean effective size $D_e$ for ice crystal as

$$D_e = \frac{\int_{L_{min}}^{L_{max}} D \cdot DLn(L)\mathrm{d}L}{\int_{L_{min}}^{L_{max}} DLn(L)\mathrm{d}L} \tag{4.17}$$

where D is the radius of an ice crystal, n(L) is the ice crystal size distribution and $L_{min}$ and $L_{max}$ are the minimum and maximum lengths of ice crystals respectively. The second one is the amount of cloud ice in the given parcel of air which is defined as Ice Water Content (IWC)

$$\mathrm{IWC} = \frac{3\sqrt{3}}{8}\rho_i \int_{L_{min}}^{L_{max}} D \cdot DLn(L)\mathrm{d}L. \tag{4.18}$$

where ice crystals are assumed to be hexagonal plates [63].

With these variables the extinction coefficient $\beta_e$, single scattering albedo $\tilde{\omega}$ and the phase function $P(\cos\theta)$ are parametrized as follows

$$\beta_e = \mathrm{IWC}\sum_{n=0}^{N} \frac{a_n}{D_e^n}, \quad \text{where IWC} = \rho_0 r_i \tag{4.19a}$$

$$1 - \tilde{\omega} = \sum_{n=0}^{N} b_n D_e^n \tag{4.19b}$$

$$P(\cos\theta) = \sum_{l=0}^{M} \tilde{\omega} P_l(\cos\theta), \quad \text{where } \tilde{\omega}_0 = 1. \tag{4.19c}$$

where the values of coefficients $a_n$ and $b_n$ can be found from the original paper [42]. The expansion coefficient $\tilde{\omega}$ in Eq. (4.19c) can be expressed by

$$\tilde{\omega} = (1 - f_\delta)\tilde{\omega}_l^* + f_\delta(2l + 1) \quad \text{for } l = 1, 2, 3, 4 \tag{4.20}$$

where $\omega_l^*$ represents the expansion coefficients for the phase function in which the forward $\delta$-function peak has been removed, and $f_\delta$ is the contribution from the forward $\delta$-function peak. The mean effective size is parametrized based on a recent Fu-Liou-Gu scheme for Cirrus clouds as follows [64]

$$\ln(D_e) = a + b\ln(\mathrm{IWC}) + c(\ln(\mathrm{IWC}))^2 \tag{4.21}$$

where the specific coefficients for Arctic are $a$ = 4.8510, $b$ = 0.331 59 and $c$ = 0.026 189.

Using Eqs. (4.19a)–(4.19c) and Eq. (4.8) for optical depth, all the radiative properties including single scattering albedo, phase function and optical depth can be calculated. These new values denoted with index n can be combined with the initial values with index i as follows

$$\tau = \tau_i + \tau_n \tag{4.22a}$$

$$\tilde{\omega} = \frac{\tilde{\omega}_i\tau_i + \tilde{\omega}_n\tau_n}{\tau_i + \tau_n} \tag{4.22b}$$

$$P(\cos\theta) = \frac{\tilde{\omega}_i\tau_i P_i(\cos\theta) + \tilde{\omega}_n\tau_n P_n(\cos\theta)}{\tilde{\omega}_i\tau_i + \tilde{\omega}_n\tau_n} \tag{4.22c}$$

With these optical properties which include the contribution of the primary gases, cloud water and ice, intensity $I$ in Eq. (4.15) can be solved using the delta-four-stream approximation and finally the radiative fluxes can be calculated from Eq. (4.16).

## 4.4 Monte Carlo spectral integration

The UCLA LES radiation model has an option to use an approximation to the spectral integration. This method is based on a Monte Carlo spectral integration(MCSI) which is an approximate method proposed for the broadband flux calculation [65].

As noted before, UCLA LES model uses the correlated k-distribution method to calculate the radiative fluxes [41]. This method divides the solar and thermal infrared spectrums into broadbands within which Rayleigh scattering by molecules and the optical properties of clouds can be considered uniform. Within each band, similar values of the absorption coefficient $k$

are grouped into "g-points" within which $k \simeq k(g)$. The broadband flux is calculated as a weighted sum of each g-point's contribution to each band.

Given that UCLA LES has 12 bands for the thermal infrared and from 3 to 12 g-points for a single gas in one band, this leads to hundreds of pseudo-monochromatic radiative flux calculations. The Monte Carlo method replaces these calculations with single randomly chosen band and g-point calculation. This is done in each vertical column of the model in every time step. This way the error that is substantial in one time step in one column of the model is uncorrelated in space and time, and it can be shown that it does not affect the statistics.

# 5 Simulation of Arctic boundary layer

## 5.1 Initial data and simulation design

To test the model, a simulation of an Arctic mixed-phase cloud was made. The initial values of the simulation were according to the case described by Morrison et al. [66]. In the study, an intercomparison between four cloud-resolving and two large-eddy simulation models was made.

The observations that were used to construct the initial values for the simulation are based on the gathered measurements from the SHEBA and from the research flights around the SHEBA site during FIRE-ACE [21][19]. The case that is used here is derived from the observations gathered from midnight to noon at local time when the measurement site was located near 76°N , 165°W. The synoptic situation consisted of a broad high-pressure zone.

The initial values of liquid water potential temperature $\theta_l$ and total water mixing ratio $r_t$ are shown in Figure 4. There is a 6.1 K temperature inversion which starts at 460 meters altitude and ends at 500 meters altitude.

In the Morrison's study the meridional and zonal winds were nudged within a timescale of 1-2 hours using the values based on the data from the European Center for Medium Range Weather Forecast (ECMWF) in order to prevent significant drift of the mean model wind [67]. In the UCLA LES version used, there was no option to nudge the variables, so instead meridional and zonal winds were put to zero. This was done also to avoid excessive wind shear. Above the inversion layer the large-scale forcing is idealized to give minimal drift of temperature and water vapor. That is for p < 95100 Pa the horizontal advective forcing of temperature and water vapor is given by

$$\left(\frac{\partial \theta_l}{\partial t}\right)_{adv} = min(1.815 \times 10^{-9}(95100 - p), 2.85 \times 10^{-5}) - 0.05\frac{R_d \theta_l}{c_p p} \quad (5.1a)$$

$$\left(\frac{\partial r_v}{\partial t}\right)_{adv} = 7 \times 10^{-7}. \quad (5.1b)$$

Here $\theta_l$ is used instead of the absolute temperature like was done in the original study, because in UCLA LES absolute temperature is diagnosed in the saturation adjustment scheme. Also the inversion pressure is 600 Pascals less in the UCLA LES model than in the original study.

Surface boundary conditions are based on the observations from the Atmospheric Surface Flux Group tower at SHEBA [68]. The surface latent and sensible turbulent heat fluxes were set to 2.86 $\mathrm{W\,m^{-2}}$ and 7.98 $\mathrm{W\,m^{-2}}$ respectively. These values were the average values during May 7th from midnight to noon in 1997. The roughness length was assumed to be $4.0 \times 10^{-4}$ m and the surface albedo of 0.827 is used. All these values were fixed during the simulation.

The models used in the Morrison's study had horizontal domains ranging from 3.2 km to 256 km and the number of vertical levels ranged from 11 to 43. One of the LES models used the Ferrier's two-moment bulk microphysical scheme [69][46] and one of the cloud resolving models used the Meyer's two-moment bulk microphysical scheme [47].

In this simulation the UCLA LES model was set to have 80 points in the horizontal domain with 35 meter spacing which is equal to 2.6 km horizontal domain. That is because 4 points are used for the overlapping. The vertical grid had 70 points with 15 meter spacing and 2% stretching started above 700 meters height. This resulted in 1.45 km high vertical grid. The simulations were done using the Aerocalc server at the Department of Applied Physics which has eight Dual-Core processors and 32 gigabytes of RAM. With this set up, one 12 hour simulation took around 7 hours to calculate.

Since the process of ice nucleation is relatively poorly constrained by observations and theory [70], the nucleation is constrained to a constant value. This way it is possible to compare the other processes between the simulations. Ice nucleation is treated diagnostically so that if $N_i$ falls below the specified $N_{IN}$ value it is nudged back to $N_{IN}$ as follows

$$\left(\frac{\partial N_i}{\partial t}\right)_{nuc} = \max(0, \frac{N_{IN} - N_i}{\Delta t}), \text{ when } S_i \geq 5,\ r_c \geq 0 \text{ and } N_i \leq N_{IN}. \tag{5.2}$$

An additional condition was to add ice only when liquid water is present, which was not used in the original study, was added. The maximum and minimum mass of the ice crystals were changed from the original values that were defined in Eq. (3.24). The new limits for ice crystal mass were

$4.73 \times 10^{-15}$ kg for the minimum $r_{i,min}$ and $1.0 \times 10^{-10}$ kg for the maximum $r_{i,max}$. In this study four sensitivity tests to the ice nuclei number concentration $N_{IN}$ were made with values $N_{IN} = 0$ m$^{-3}$, $N_{IN}$=170 m$^{-3}$, $N_{IN}$=1700 m$^{-3}$ and $N_{IN}$=5100 m$^{-3}$. The results are presented and discussed in the following sections. In addition there was one simulation with $N_{IN}$=1700 m$^{-3}$ where the full radiation model was used without the Monte Carlo spectral integration and one with finer vertical grid (110 vertical levels).

## 5.2 Thermodynamic profiles

Horizontally-averaged profile of liquid water potential temperature $\theta_l$, total water mixing ratio $r_t$, cloud water mixing ratio $r_c$ and cloud ice mixing ratio $r_i$ averaged from the last 30 minutes of the simulation together with the specified initial condition are shown in Figure 4. Due to strong thermal and mechanical turbulence at noon, the boundary layer is well-mixed, meaning that the $r_t$ and $\theta_l$ are fairly uniform in the end of the simulation. Although in the high $N_{IN}$ case the $r_t$ shows a decrease due to altitude, which might be because the $r_t$ does not include ice. The reason for this is that the saturation adjustment scheme used in the UCLA LES was using the total water mixing ratio in a way that simple addition of ice would have not given sensible results.

There is a difference in $\theta_l$ between the low and high ice nuclei concentration simulations. The boundary layer is warming more in the high $N_{IN}$ simulations because of the latent heat release due to depositional growth and due to the radiative heating.

The surface value of total water mixing ratio increases roughly 0.2 g kg$^{-1}$. This is due to the constant latent heat flux of 7.98 W m$^{-2}$. Looking at $r_l$ it is clear that in the warm phase case there is a liquid cloud top at the boundary layer. For the $N_{in} = 1700$ m$^{-3}$ case there is a mixed-phase cloud with maximum of 0.03 g kg$^{-1}$ of liquid water and maximum of 0.006 g kg$^{-1}$ of ice at the surface. Similarly for the $N_{in} = 170$ m$^{-3}$case there is 0.21 g kg$^{-1}$ of liquid water and 0.001 g kg$^{-1}$ of ice at the surface. For the very high ice nuclei concentration case there is almost no liquid water at the end of simulation.

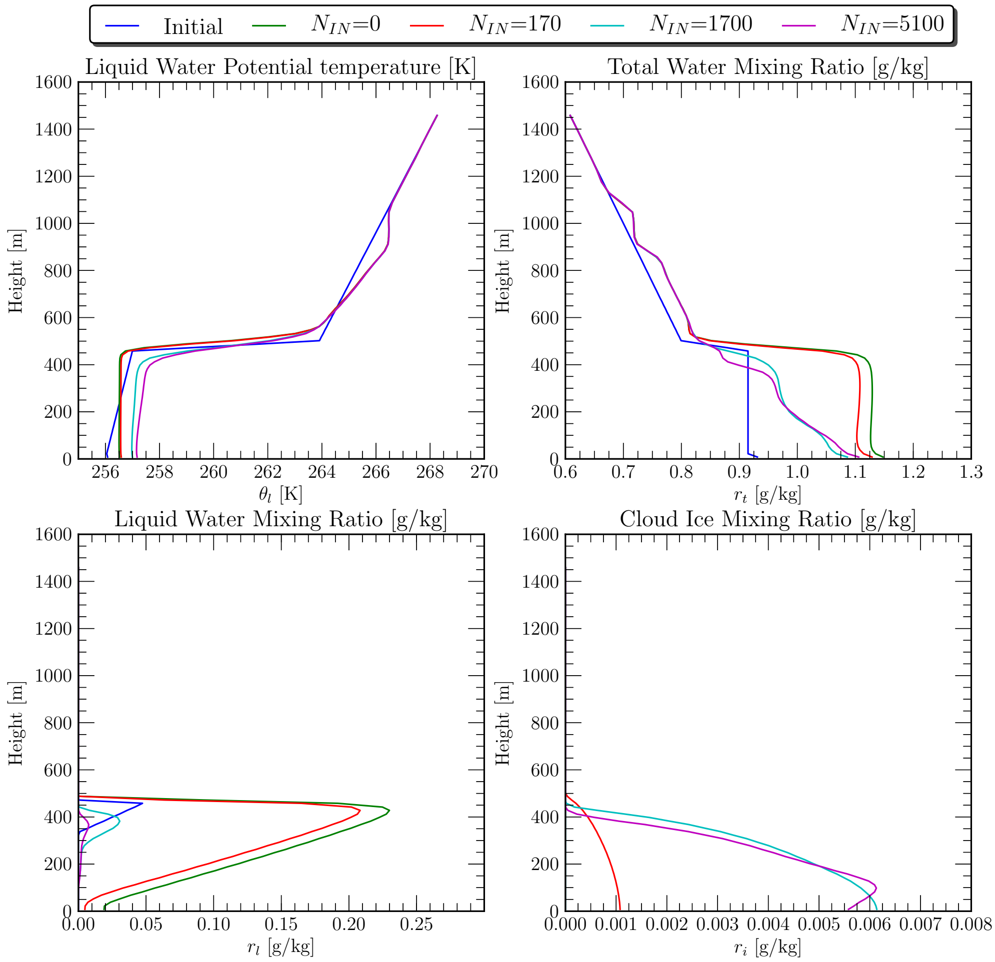


Figure 4: Horizontally averaged vertical profiles $\theta_l$, $r_t$, $r_c$ and $r_i$ in the end of simulation averaged from the last 30 minutes.

It is important to note that in these simulations the ice crystal number concentration $N_i$ was not a constant value although it was meant to stay constant using the above mentioned ice nucleation scheme. This is illustrated in Figure 5. The ice crystal number concentration is zero during the first hour because the ice nucleation process was started only after the initial model spin-up of one hour. This approach was not used by Morrison et al. but it was suggested to be used in the future simulations.

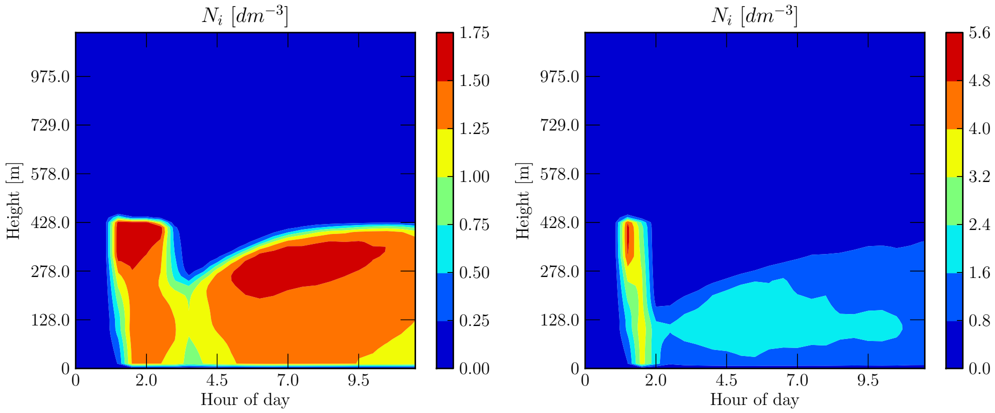


Figure 5: Evolution of $N_i$ concentration for initial concentration of $N_i = 1700$ m$^{-3}$ and $N_i = 5100$ m$^{-3}$.

In the first figure for $N_{IN}$=1700 m$^{-3}$ case, ice stays constant for 2 hours after the first hour. After that there is a sharp decrease to zero. This happens because there is no liquid water present anymore. Thus, according to Eq. (5.2) no ice is added to the boundary layer. Liquid water is available again later due to the saturation adjustment after which ice nucleation continues. In the second figure the decrease is even more striking because all of the liquid water is depleted after the model spin-up and no nucleation happens after the first initial addition of ice. The difference between the $N_{IN}$=1700 m$^{-3}$ case and $N_{IN}$=5100 m$^{-3}$ case is that for $N_{IN}$=1700 m$^{-3}$ simulation the ice crystal number concentration stays close to the value 1700 m$^{-3}$ in the boundary layer while for the $N_{IN}$=5100 m$^{-3}$ simulation the ice crystal number concentration is close to 2000 m$^{-3}$.

To take a closer look at the evolution of the liquid water mixing ratio and cloud ice mixing ratio, the timeseries of the horizontally-averaged profiles are plotted. In Figure 6 there are the timeseries of the horizontally averaged vertical profile for $r_l$ and $r_i$ for the $N_{IN}$ = 170 m$^{-3}$ simulation. From the first figure it can be seen that the liquid water cloud is growing throughout the simulation. This is due to the rising thermals and mixing from the boundary layer which make the air saturated. At the same time, ice is forming due to the water vapor deposition but because of the low concentration of initial ice nuclei, the amount of ice stays low.

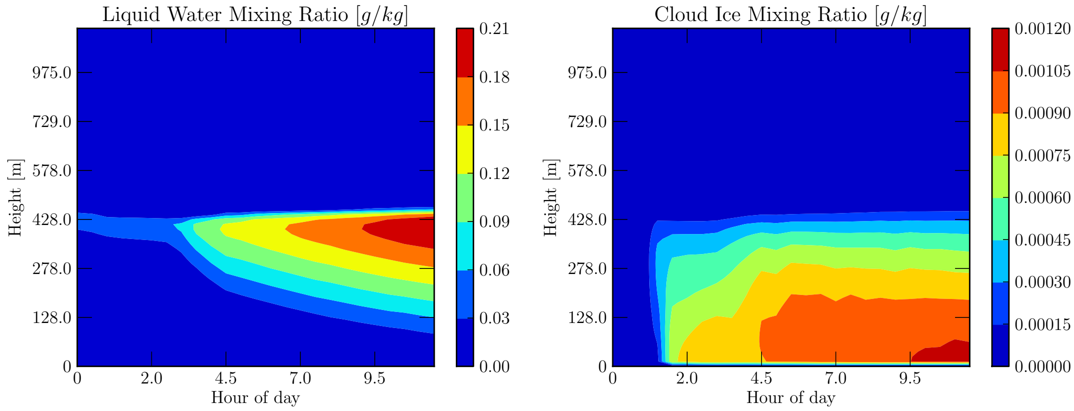


Figure 6: Timeseries of horizontally averaged vertical profiles of $r_l$ and $r_i$ in the $N_{IN} = 170$ m$^{-3}$ case.

In Figure 7 there are the timeseries of the horizontally averaged vertical profiles for $r_l$ and $r_i$ for the $N_{IN} = 1700$ m$^{-3}$ simulation. In the first figure the already mentioned decrease of liquid water after 2 hours of simulation is evident. This decrease has also an influence to the amount of ice. It has to be noted that the color bars in Figures 6 and 7 are not equal. By roughly comparing the cloud ice figures it can be seen that the there is approximately seven times more ice in the $N_{IN} = 1700$ m$^{-3}$ simulation. Also, in both figures a blue line at the surface can be seen which is the surface boundary. This means that the ice coming all the way down to the surface will be removed from the simulation.

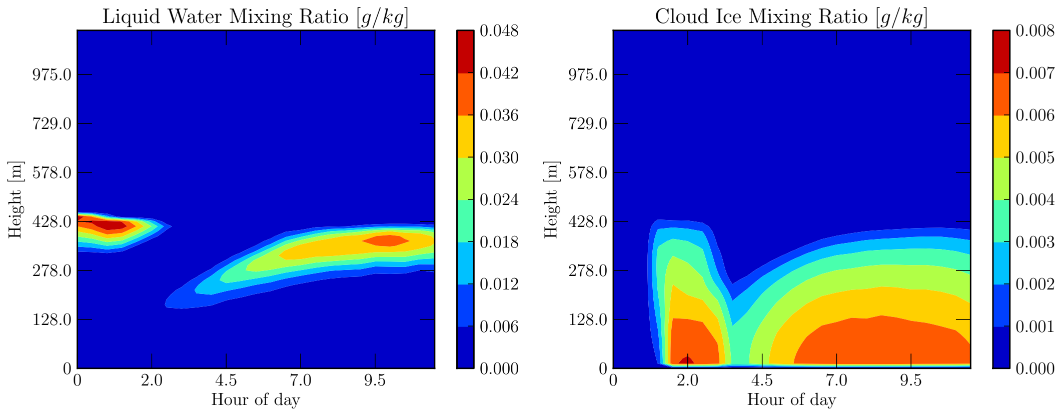


Figure 7: Timeseries of horizontally averaged vertical profiles of $r_l$ and $r_i$ in the $N_{IN} = 1700$ m$^{-3}$ case.

Time evolution of horizontally-averaged LWP, RWP, IWP and the total value of turbulent kinetic energy at the height of 202 meters are shown in Figure 8. There is a sharp decrease in the LWP for the higher $N_{IN}$ simulations (red and turquoise lines) after the first hour and at the same time there is a sharp increase in the IWP in these simulations. This is glaciation of liquid water which happens because the ice is growing fast due to water vapor deposition which results to decrease in water vapor. This in turn leads to evaporation of liquid water. That is to say that, the ice is growing at the expense of water vapor and liquid water.

From the RWP plot it can be seen that there was very little rain forming in the liquid clouds. In the simulations without ice, RWP was peaking at 0.0006 g m$^{-2}$. On the other hand there was ice preciptation which is show in Figure 9. After the initial ice nucleation, the horizontally averaged surface ice precipitation rate attain a value of 0.02 g kg$^{-1}$ m s$^{-1}$ for $N_{IN}$=1700 m$^{-3}$ and $N_{IN}$=5100 m$^{-3}$ cases. This happens because the ice crystal concentration has similar values after the initial ice nucleation which can be seen in Figure 5.

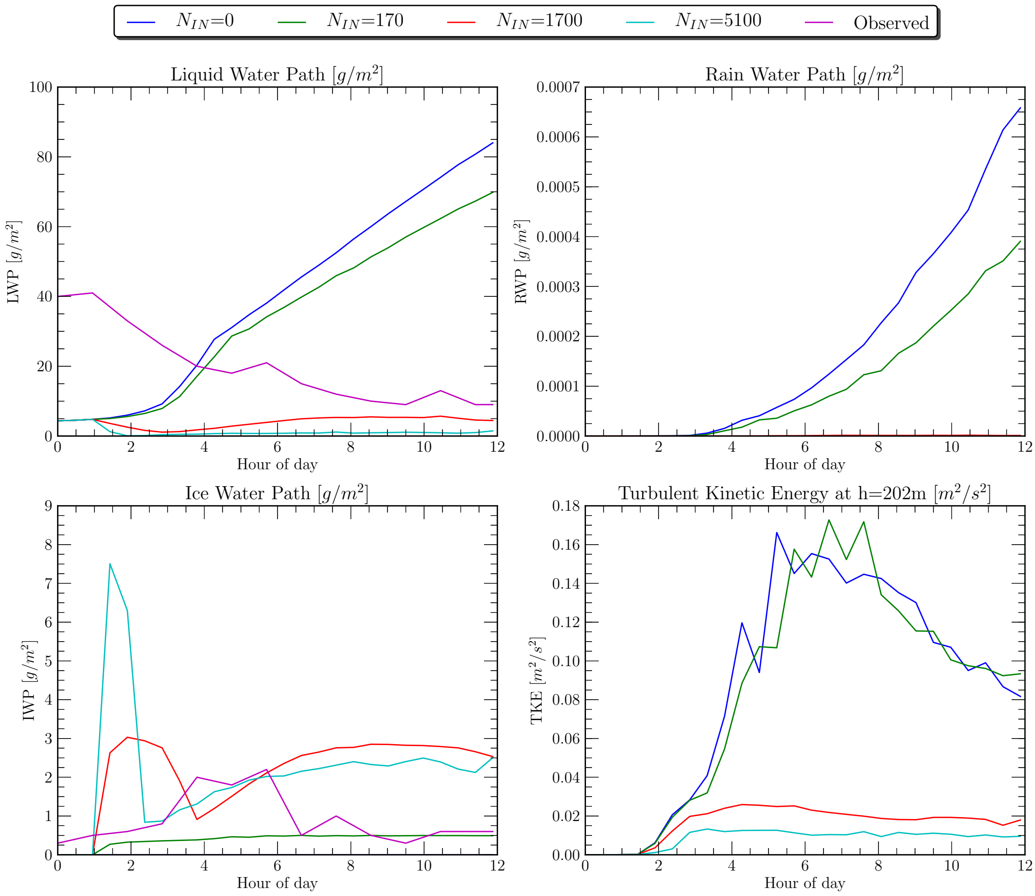


Figure 8: Time series for modeled and observed LWP, RWP, IWP and TKE. TKE is measured at height of 202 meters.

The Turbulent Kinetic Energy (TKE) in Figure 8 is much higher for the liquid water clouds than for the ice clouds. This is because the water loading in the buoyancy equation Eq. (2.6), is higher for ice which in turn makes the buoyancy smaller. Also, the dynamics is fully-developed in high $N_{IN}$ simulations because the TKE has almost constant value after first 3 hours of simulation time. Liquid water clouds simulations have much higher TKE value which is explained by higher concentration of liquid water. This in turn results in stronger cloud top radiative cooling and higher TKE.

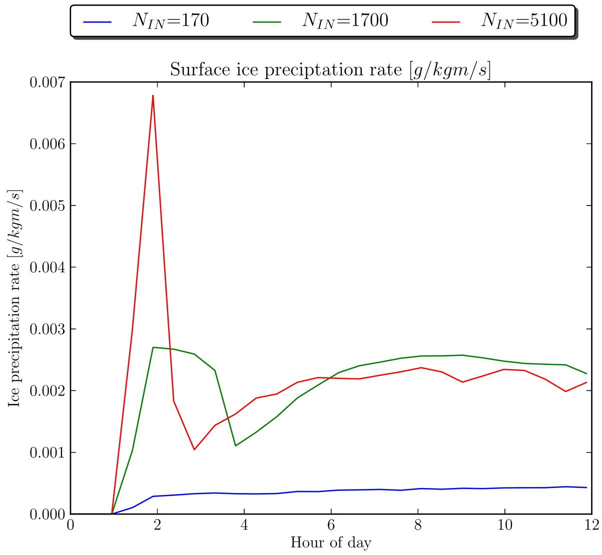


Figure 9: Timeseries of horizontally averaged surface ice precipitation rate for $N_{IN}$=170 m$^{-3}$, $N_{IN}$=1700 m$^{-3}$ and $N_{IN}$=5100 m$^{-3}$.

A simulation with 110 vertical levels with the same initial conditions as the $N_{IN}$=1700 m$^{-3}$ was made to study sensitivity of the simulation to the vertical grid spacing. In Figure 10 there are the variance of the vertical wind and the buoyancy production of resolved TKE which is defined as the correlation of the buoyancy Eq. (2.6) and the vertical wind. These figures show that in the boundary layer (height less than 500 meters) the finer grid has weaker vertical wind.

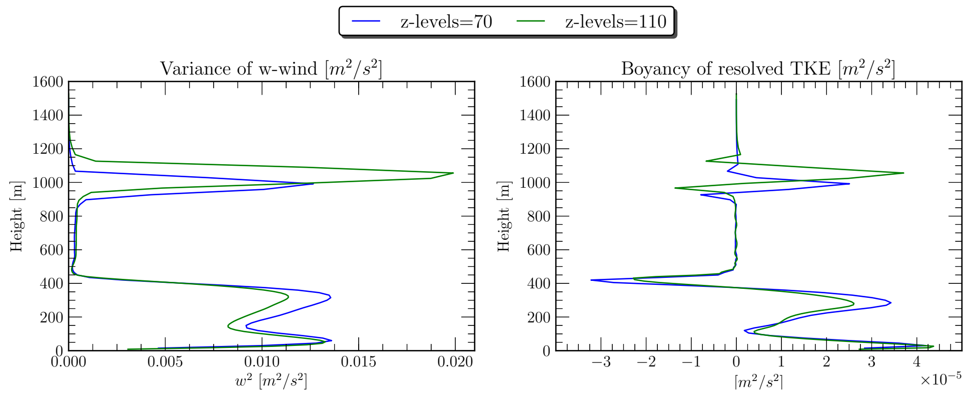


Figure 10: Variance of w-wind and buoyancy production of resolved TKE for $N_{IN}$=1700 m$^{-3}$ and z-levels 70 and 110.

## 5.3 Surface radiative fluxes

In this section the radiative characteristics of the simulations are presented. In Figure 11 there is horizontally-averaged values of down welling surface fluxes for the shortwave (SW) and longwave (LW) radiation. Downward shortwave flux is 175 W m$^{-2}$ higher for the $N_{IN}$=1700 m$^{-3}$ simulation compared to the $N_{IN}$=170 m$^{-3}$ simulation. On the other hand, downward longwave radiation is 22.5 W m$^{-2}$ lower for the $N_{IN}$=1700 m$^{-3}$ simulation compared to the $N_{IN}$=170 m$^{-3}$ simulation. This shows that the ice clouds are optically thinner than the liquid water clouds and that the downward radiative fluxes are mainly depended on the liquid water content of the cloud.

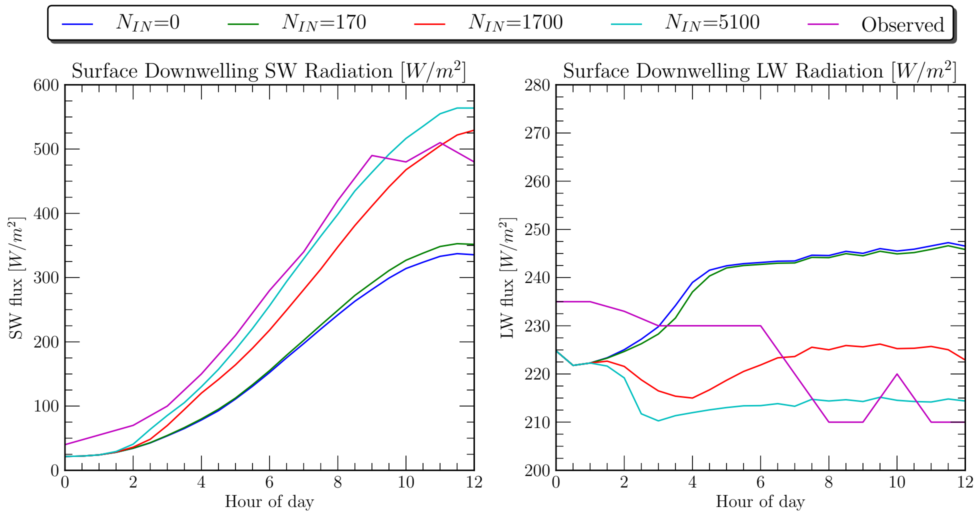


Figure 11: Horizontally-averaged downwelling surface fluxes.

To evaluate the error induced by using the Monte Carlo spectral integration in the simulations, a full radiation calculation was made with $N_{IN}$=1700 m$^{-3}$. Comparison between the horizontally-averaged downwelling shortwave and longwave fluxes for these simulations are shown in the Figure 12. From the longwave radiation figure it can be seen that at the first time step the difference is 3 W m$^{-2}$ and it is less than that during the rest of the simulation. The advantage of Monte Carlo method is that it is coputationally much more efficient. For these simulations the calculation of one time step took on the average 2 seconds using Monte Carlo method and 25 seconds using the full radiation method.

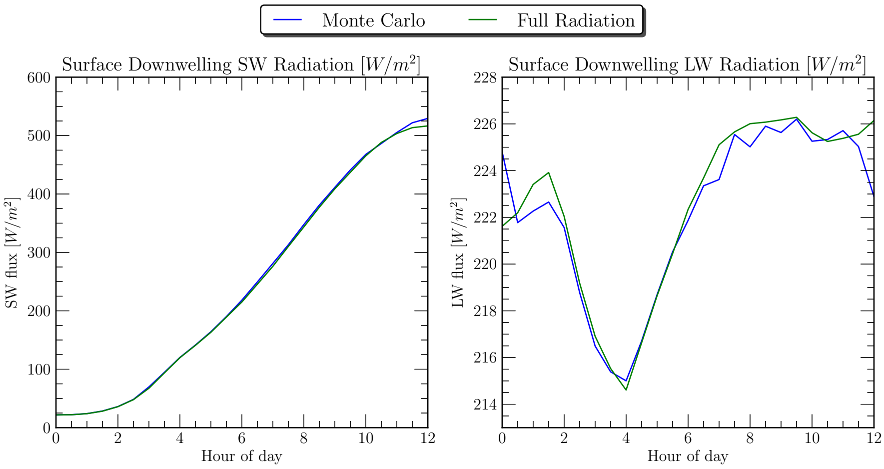


Figure 12: Comparison of the Monte Carlo method and full radiation method for $N_{IN}$=1700 m$^{-3}$.

## 5.4 Summary

Four simulations with varying amount of ice nuclei were performed. In addition, the full radiation method was compared against the Monte Carlo method and a sensitivity test to the vertical grid spacing was made.

As pointed out by Morrison et al. this case had limited riming, aggregation and ice crystal sublimation which reduced the microphysical complexity of the simulations. The UCLA LES model used in this study did not include the ice crystal riming or aggregation but those processes probably would have not changed the results dramatically. Ice was growing mainly due to the water vapor deposition. The depositional growth rate had peak values of $2.1 \times 10^{-6}$ g kg$^{-1}$ s$^{-1}$, $2.1 \times 10^{-5}$ g kg$^{-1}$ s$^{-1}$ and $6.0 \times 10^{-5}$ g kg$^{-1}$ s$^{-1}$ for $N_{IN}$=170 m$^{-3}$, $N_{IN}$=1700 m$^{-3}$ and $N_{IN}$=5100 m$^{-3}$, respectively. It was concluded in original study that the mean values of 1–2 $\times 10^{-6}$ g kg$^{-1}$ s$^{-1}$ of the depositional growth appeared to results in rapid glaciation of cloud in most of the models. Although this limit can vary between the models, in this case it also resulted into rapid glaciation as seen from the thermodynamic profiles for the $N_{IN}$=1700 m$^{-3}$ case. The depositional growth is a strong function of the terminal fall speed of the ice crystal and it was difficult to get realistic values for the fall speed. Because of this, the ventilation coefficient in Eq. (3.19) was assumed to be 1.0. The production of ice due to freezing of cloud water was minimal during all the simulations. For the $N_{IN}$=1700 m$^{-3}$ simulation, the freezing rate was peaking at $8.0 \times 10^{-9}$ g kg$^{-1}$ s$^{-1}$ and in the $N_{IN}$=170 m$^{-3}$ case, the freezing rate had a peak value of $1.4 \times 10^{-7}$ g kg$^{-1}$ s$^{-1}$ in the end of simulation.

It was found that a higher initial concentration of ice crystals lead to faster glaciation of the cloud. By comparing the simulations with different ice crystal concentration, two different types of clouds were observed. Lower ice crystal concentration led to stable mixed-phase cloud and higher ice crystal concentration led to all ice cloud. This result was also found in the original study by Morrison et al. [66]. Similar result has also been found by Harrington et al. when they used cloud-resolving model simulations to show that a largely liquid Arctic stratus deck can be transformed into a broken optically-thin ice cloud by modest increases of ice nuclei concentrations [6]. In another simulation they also found that the boundary layer with mixed-phase clouds had weaker convection and shallower boundary layer depth than boundary layers with liquid water only [71]. Weaker convection is due to strong ice precipitation which reduces convective strength directly by stabilizing downdrafts and more indirectly by sensible heating of the boundary layer and inhibiting vertical mixing of momentum there by reducing surface heat fluxes. This was also found in the UCLA LES model simulations. The reduced boundary layer depth in the high $N_{IN}$ case can be seen in the end profile of $\theta_l$ in Fig. 4 and the weaker convection is confirmed by much higher variance of vertical wind in the simulation with low ice nuclei concentration.

Simulations with mixed-phase clouds had larger surface downward longwave and smaller shortwave fluxes compared to the rapidly glaciated all-ice clouds. As expected, all-ice clouds are optically thinner than mixed-phase clouds and the radiative properties of the clouds are highly dependent on the liquid water content of the clouds.

The Monte Carlo spectral integration method had a maximum deviation of 3 W m$^{-2}$ when the full radiation method was used. This error is less than or equal to the systematic error in the radiative scheme, bias in subgrid scale model or uncertain representation of microphysical processes [65]. Thus it can be concluded that Monte Carlo method was suitable for these simulations. The advantage of it is the significantly reduced computational cost in the radiation calculation.

The sensitivity of the simulation to the vertical grid spacing might be because of the sub-grid scale model used. The Smagorinsky model which was used in these simulations has been found to be very sensitive to vertical grid spacing [37].

# 6 Conclusions

Simulations of the Arctic mixed-phase boundary layer cloud were made. The work also included the addition of ice microphysical processes and a parametrization of radiative properties of ice crystals to the existing UCLA LES model.

The existing microphysical scheme was extended to include nucleation of the ice, cloud water and rain water freezing, growth of ice by water vapor deposition and sedimentation. To constrain the ice nucleation process, the ice nuclei concentration was fixed during the simulations. This enabled to do sensitivity tests of the ice nuclei concentrations with values of $N_{IN} = 0$ m$^{-3}$, $N_{IN} = 170$ m$^{-3}$, $N_{IN} = 1700$ m$^{-3}$ and $N_{IN} = 5100$ m$^{-3}$. The nucleation scheme could have been better tuned for the UCLA LES model because in the $N_{IN} = 5100$ m$^{-3}$ simulation, the value of ice crystal concentration was only around 2000 m$^{-3}$ instead of 5100 m$^{-3}$. Between the different simulations there were significant differences in the radiative fluxes and in the amount of liquid water and ice. High ice nuclei concentration led to rapid glaciation of the liquid water whereas in the cases $N_{IN} = 0$ m$^{-3}$ and $N_{IN} = 170$ m$^{-3}$, a persistent mixed-phase cloud was observed.

The mixed-phased clouds had weaker convection and shallower boundary layer depth than the liquid water clouds. This is because the ice precipitation reduces convective strength by stabilizing downdrafts. Also in the case of mixed-phase clouds, there is sensible heating of the boundary layer which inhibits vertical mixing of momentum thereby reducing surface fluxes.

Only parts of the SB model were implemented because the complete SB model is very complicated. This approach was probably adequate for this simulation case which had limited riming, aggregation and ice crystal sublimation. The complexity of the microphysical model depends always on the examined problem. If an individual cloud and the aerosol effects on the cloud are studied then a detailed microphysical model is needed. However, for a study of average precipitation on a mesoscale region a simpler microphysical model is sufficient.

It is important to realize that the theory of the mixed-phase clouds is not yet well understood and there are many problems related to modeling them.

The assumptions made in extending the Kessler approach to the ice phase is questionable because in the original Kessler scheme for warm clouds, the supersaturation with respect to water is believed to be less than 1 % while the supersaturation with respect to ice can be close to 20 %. For warm phase clouds all the saturated water is assumed to be cloud water while for cold clouds all the saturated ice cannot be cloud ice. The saturation adjustment is further complicated when multiple categories of ice are present and the saturated ice has to be partioned to each category.

Recently attempts to avoid the shortcomings of the Kessler approach for the bulk ice microphysics have been made. To retain a substantial amount of the supersaturation of ice, Cotton et al. replaced the concept of "cloud ice" with predicted pristine ice which is an ice category that is purely grown by water vapor deposition [72]. Another approach was introduced by Morrison and Grobowski in which all ice microphysical processes and parameters are calculated in terms of mass-dimension, area-dimension relationships and number concentration of ice particles. This approach does not separate ice into predefined categories of ice and thus avoids the problems of transitions between the different categories [73].

In terms of the LES models in general, they are suitable for modelling specific boundary layer clouds. The most challenging processes to model are: radiation (which is at best two-dimensional), microphysics, atmospheric chemistry, aerosols and surface fluxes. In addition, numerical issues are always present when representing numbers on a computer with limited precision.

Although the UCLA LES model is little over 10000 lines of codes, it is still relatively easy to understand and modify compared to the larger models like Weather Research and Forecasting (WRF) model. Most importantly, it was easy to make new model variables to get more information on a specific process. The development of UCLA LES model is continuing in the Max Planck Institute for Meteorology. The model provides a relatively easy platform to do LES simulations and to extend its capabilities. For example, the microphysics module could be replaced by an explicit bin microphysical model. The advantage of the bin microphysical scheme is that it does not assume a certain shape for the particle distribution in contrast to the bulk microphysical scheme. This can be an important factor since the observed particles do behave like some known distribution but the deviation from this distribution is the key in initiating some microphysical process.

# References


[1] R. Pachauri, *Climate Change 2007: Synthesis Report. Contribution of Working Groups I, II and III to the Fourth Assessment Report of the Intergovernmental Panel on Climate Change*, Vol. 446, (IPCC, 2007).

[2] European Meteorological Institutes, "High Resolution Limited Area Model (HIRLAM)," `www.hirlam.org` (2012).

[3] S. Solomon, *Climate Change 2007: The Physical Science Basis: Contribution of Working Group I to the Fourth Assessment Report of the Intergovernmental Panel on Climate Change* (Cambridge University Press, 2007).

[4] D. Randall, J. Curry, D. Battisti, G. Flato, R. Grumbine, S. Hakkinen, D. Martinson, R. Preller, J. Walsh, and J. Weatherly, "Status of and outlook for large-scale modeling of atmosphere-ice-ocean interactions in the Arctic," *Bulletin of the American Meteorological Society* **79,** 197–220 (1998).

[5] P. Olsson, J. Harrington, G. Feingold, W. Cotton, and S. Kreidenweis, "Exploratory cloud-resolving simulations of boundary-layer Arctic stratus clouds:: Part I: Warm-season clouds," *Atmospheric Research* **47,** 573–597 (1998).

[6] J. Harrington, T. Reisin, W. Cotton, and S. Kreidenweis, "Cloud resolving simulations of Arctic stratus:: Part II: Transition-season clouds," *Atmospheric Research* **51,** 45–75 (1999).

[7] Y. Luo, K. Xu, H. Morrison, and G. McFarquhar, "Arctic mixed-phase clouds simulated by a cloud-resolving model: Comparison with ARM observations and sensitivity to microphysics parameterizations," *Journal of the Atmospheric Sciences* **65,** 1285–1303 (2008).

[8] J. Fan, M. Ovtchinnikov, J. Comstock, S. McFarlane, and A. Khain, "Ice formation in Arctic mixed-phase clouds: Insights from a 3-D cloud-resolving model with size-resolved aerosol and cloud microphysics," *Journal of Geophysical Research* **114,** D04205 (2009).

[9] S. Klein, R. McCoy, H. Morrison, A. Ackerman, A. Avramov, G. Boer, M. Chen, J. Cole, A. Del Genio, M. Falk, et al., "Intercomparison of model simulations of mixed-phase clouds observed during the ARM Mixed-Phase Arctic Cloud Experiment. I: single-layer cloud," *Quarterly Journal of the Royal Meteorological Society* **135,** 979–1002 (2009).

[10] H. Morrison and J. Pinto, "Intercomparison of bulk cloud microphysics schemes in mesoscale simulations of springtime Arctic mixed-phase stratiform clouds," *Monthly Weather Review* **134,** 1880–1900 (2006).

[11] R. Stull, *An Introduction to Boundary Layer Meteorology*, Vol. 13, (Springer, 1988).

[12] W. Cotton, *Storm and Cloud Dynamics*, Vol. 99, (Academic press, 2010).

[13] J. Curry, W. Rossow, D. Randall, and J. Schramm, "Overview of Arctic cloud and radiation characteristics," *Journal of Climate* **9,** 1731–1764 (1996).

[14] K. Mcinnes and J. Curry, "Modelling the mean and turbulent structure of the summertime Arctic cloudy boundary layer," *Boundary-Layer Meteorology* **73,** 125–143 (1995).

[15] H. Diaz, "Climatology of surface-based inversions in the North American Arctic," *Journal of Geophysical Research* **97,** 15–699 (1992).

[16] J. Paatero, P. Vaattovaara, M. Vestenius, O. Meinander, U. Makkonen, R. Kivi, A. Hyvärinen, E. Asmi, M. Tjernström, and C. Leck, "Finnish contribution to the Arctic Summer Cloud Ocean Study (ASCOS) expedition, Arctic Ocean 2008," *Geophysica* **45,** 119–146 (2009).

[17] G. Stokes and S. Schwartz, "The Atmospheric Radiation Measurement (ARM) Program: Programmatic background and design of the cloud and radiation test bed," *Bulletin of the American Meteorological Society* **75** (1994).

[18] G. McFarquhar, S. Ghan, J. Verlinde, A. Korolev, J. Strapp, B. Schmid, J. Tomlinson, M. Wolde, S. Brooks, D. Cziczo, et al., "Indirect and semi-direct aerosol campaign: The impact of Arctic aerosols on clouds," *Bulletin of the American Meteorological Society* **92,** 183–201 (2011).

[19] J. Curry, P. Hobbs, M. King, D. Randall, P. Minnis, G. Isaac, J. Pinto, T. Uttal, A. Bucholtz, D. Cripe, et al., "FIRE Arctic clouds experiment," *Bulletin of American Meteorological Society* **81,** 5–30 (2000).

[20] J. Verlinde, J. Harrington, G. McFarquhar, V. Yannuzzi, A. Avramov, S. Greenberg, N. Johnson, G. Zhang, M. Poellot, J. Mather, et al., "The mixed-phase Arctic cloud experiment," *Bulletin of the American Meteorological Society* **88,** 205–222 (2007).

[21] T. Uttal, J. Curry, M. Mcphee, D. Perovich, R. Moritz, J. Maslanik, P. Guest, H. Stern, J. Moore, R. Turenne, et al., "Surface heat budget of the Arctic Ocean," *Bulletin of the American Meteorological Society* **83,** 255–275 (2002).

[22] J. Straka, *Cloud and Precipitation Microphysics: Principles and Parameterizations* (Cambridge, 2009).

[23] The University of Manchester, "Ice crystal morphology diagram," `http://www.cas.manchester.ac.uk/resactivities/cloudphysics/topics/lightscattering/` (2012).

[24] J. Straka and E. Mansell, "A bulk microphysics parameterization with multiple ice precipitation categories," *Journal of Applied Meteorology* **44,** 445–466 (2005).

[25] R. Goody and Y. Yung, *Atmospheric Radiation: Theoretical Basis* (Oxford University Press, USA, 1995).

[26] K. Liou, *An Introduction to Atmospheric Radiation*, Vol. 84, (Academic Pr, 2002).

[27] J. Seinfeld and P. S.N, *Atmospheric Chemistry and Physics. From Air Pollution to Climate Change. 2nd edition.* (John Wiley & Sons, Inc., 2006).

[28] A. Tsonis, *An Introduction to Atmospheric Thermodynamics* (Cambridge University Press, 2002).

[29] J. Holton, *An Introduction to Dynamic Meteorology*, Vol. 1, (Academic Press, 2004).

[30] K. Emanuel, *Atmospheric Convection* (Oxford University Press, USA, 1994).

[31] B. Stevens, "Atmospheric moist convection," *Annual Review of Earth and Planetary Sciences* **33,** 605–643 (2005).

[32] D. Tritton, *Physical Fluid Dynamics* (Oxford, Clarendon Press, 1988, 536 p., 1988).

[33] T. Heus, C. Van Heerwaarden, H. Jonker, A. Siebesma, S. Axelsen, K. van den Dries, O. Geoffroy, A. Moene, D. Pino, S. de Roode, and J. Vila-Guerau de Areliano, "Formulation of and numerical studies with the Dutch Atmospheric Large-Eddy Simulation (DALES)," *Geoscientific Model Development Discussion* **3,** 99–180 (2010).

[34] C. Moeng, "A large-eddy-simulation model for the study of planetary boundary-layer turbulence," *Journal of the Atmospheric Sciences* **41,** 2052–2062 (1984).

[35] B. Stevens, "Introduction to UCLA-LES version 3.2.1," (2010).

[36] J. Smagorinsky, "General circulation experiments with the primitive equations," *Monthly Weather Review* **91,** 99–164 (1963).

[37] B. Stevens, C. Moeng, and P. Sullivan, "Large-eddy simulations of radiatively driven convection: Sensitivities to the representation of small scales," *Journal of the Atmospheric Sciences* **56,** 3963–3984 (1999).

[38] The Max Planck Institute for Meteorology, "The UCLA Large Eddy Simulation Code," `http://www.mpimet.mpg.de/en/science/the-atmosphere-in-the-earth-system/working-groups/clouds-and-convection/large-eddy-simulations.html` (2012).

[39] B. Van Leer, "Towards the ultimate conservative difference scheme III. Upstream-centered finite-difference schemes for ideal compressible flow," *Journal of Computational Physics* **23,** 263–275 (1977).

[40] K. Liou, Q. Fu, and T. Ackerman, "A simple formulation of the delta-four-stream approximation for radiative transfer parameterizations," *Journal of the Atmospheric Sciences* **45,** 1947 (1988).

[41] Q. Fu and K. Liou, "On the correlated k-distribution method for radiative transfer in nonhomogeneous atmospheres," *Journal of the Atmospheric Sciences* **49,** 2139–2156 (1992).

[42] F. Qiang and K. Liou, "Parameterization of radiative properties of cirrus clouds," *Journal of the Atmospheric Sciences* **50,** 2008–2025 (1993).

[43] A. Seifert and K. Beheng, "A two-moment cloud microphysics parameterization for mixed-phase clouds. Part 1: Model description," *Meteorology and atmospheric physics* **92,** 45–66 (2006).

[44] E. Kessler, "On the distribution and continuity of water substance in atmospheric circulations," *Meteorological Monograph 32.* (1969).

[45] S. Rutledge and P. Hobbs, "The mesoscale and microscale structure and organization of clouds and precipitation in midlatitude cyclones. XII- A diagnostic modeling study of precipitation development in narrow cold-frontal rainbands," *Journal of the Atmospheric Sciences* **41,** 2949–2972 (1984).

[46] B. Schoenberg Ferrier, "A double-moment multiple-phase four-class bulk ice scheme. Part I: Description," *Journal of the Atmospheric Sciences* **51,** 249–280 (1994).

[47] M. Meyers, R. Walko, J. Harrington, and W. Cotton, "New RAMS cloud microphysics parameterization. Part II: The two-moment scheme," *Atmospheric Research* **45,** 3–39 (1997).

[48] J. Reisner, R. Rasmussen, and R. Bruintjes, "Explicit forecasting of supercooled liquid water in winter storms using the MM5 mesoscale

model," *Quarterly Journal of the Royal Meteorological Society* **124,** 1071–1107 (1998).

[49] A. Khain, M. Ovtchinnikov, M. Pinsky, A. Pokrovsky, and H. Krugliak, "Notes on the state-of-art numerical modeling of cloud microphysics," *Atmospheric Research* **55,** 159–224 (2000).

[50] J. Hallett, "Production of secondary ice particles during the riming process," *Nature* **249,** 26–28 (1974).

[51] S. Mossop, "Production of secondary ice particles during the growth of graupel by riming," *Quarterly Journal of the Royal Meteorological Society* **102,** 45–57 (1976).

[52] M. Meyers, P. Demott, and W. Cotton, "New primary ice-nucleation parameterizations in an explicit cloud model," *Journal of Applied Meteorology* **31,** 708–721 (1992).

[53] E. Bigg, "The formation of atmospheric ice crystals by the freezing of droplets," *Quarterly Journal of the Royal Meteorological Society* **79,** 510–519 (1953).

[54] C. Wisner, H. Orville, and C. Myers, "A numerical model of a hail-bearing cloud," *Journal of the Atmospheric Sciences* **29,** 1160–1181 (1972).

[55] A. Korolev, "Limitations of the Wegener-Bergeron-Findeisen mechanism in the evolution of mixed-phase clouds," *Journal of the Atmospheric Sciences* **64,** 3372–3375 (2007).

[56] W. Cotton, G. Tripoli, R. Rauber, and E. Mulvihill, "Numerical simulation of the effects of varying ice crystal nucleation rates and aggregation processes on orographic snowfall," *Journal of Climate and Applied Meteorology* **25,** 1658–1680 (1986).

[57] F. Murray, "On the computation of saturation vapor pressure.," *Journal of Applied Meteorology* **6,** 203–204 (1966).

[58] A. Heymsfield and M. Kajikawa, "An improved approach to calculating terminal velocities of plate-like crystals and graupel.," *Journal of Atmospheric Sciences* **44,** 1088–1099 (1987).

[59] A. Seifert and K. Beheng, "A double-moment parameterization for simulating autoconversion, accretion and selfcollection," *Atmospheric research* **59,** 265–281 (2001).

[60] R. Rogers and Y. M.K., *A Short Course in Cloud Physics.* (Butterworth-Heinemann, 1989).

[61] B. Stevens and A. Seifert, "Understanding macrophysical outcomes of microphysical choices in simulations of shallow cumulus convection," *Journal of the Meteorological Society of Japan* **86,** 143–162 (2008).

[62] K. Liou, "Analytic two-stream and four-stream solutions for radiative transfer," *Journal of Atmospheric Sciences* **31,** 1473 (1974).

[63] Q. Fu, P. Yang, and W. Sun, "An accurate parameterization of the infrared radiative properties of cirrus clouds for climate models," *Journal of Climate* **11,** 2223–2237 (1998).

[64] Y. Gu, K. Liou, S. Ou, and R. Fovell, "Cirrus cloud simulations using WRF with improved radiation parameterization and increased vertical resolution," *Journal of Geophysical Research* **116,** D06119 (2011).

[65] R. Pincus and B. Stevens, "Monte Carlo spectral integration: A consistent approximation for radiative transfer in large eddy simulations," *Journal of Advances in Modeling Earth Systems* **1,** 9 (2009).

[66] H. Morrison11, P. Zuidema, A. Ackerman, A. Avramov, G. de Boer, J. Fan, A. Fridlind, T. Hashino, J. Harrington, Y. Luo, et al., "Intercomparison of cloud model simulations of Arctic mixed-phase boundary layer clouds observed during SHEBA/FIRE-ACE," *Journal of Advances in Modeling Earth Systems* **3,** M05001 (2011).

[67] H. Morrison and J. Pinto, "A new approach for obtaining advection profiles: Application to the SHEBA column," *Monthly weather review* **132,** 687–702 (2004).

[68] P. Persson, C. Fairall, E. Andreas, P. Guest, and D. Perovich, "Measurements near the Atmospheric Surface Flux Group tower at SHEBA: Near-surface conditions and surface energy budget," *Journal of Geophysical Research* **107** (2002).

[69] G. Shutts and M. Gray, "A numerical modelling study of the geostrophic adjustment process following deep convection," *Quarterly Journal of the Royal Meteorological Society* **120,** 1145–1178 (1994).

[70] A. Fridlind, A. Ackerman, G. McFarquhar, G. Zhang, M. Poellot, P. DeMott, A. Prenni, and A. Heymsfield, "Ice properties of single-layer stratocumulus during the Mixed-Phase Arctic Cloud Experiment: 2. Model results," *Journal of Geophysical Research* **112,** D24202 (2007).

[71] J. Harrington and P. Olsson, "On the potential influence of ice nuclei on surface-forced marine stratocumulus cloud dynamics," *Journal of Geophysical Research* **106,** 27473–27484 (2001).

[72] W. Cotton, R. Pielke Sr, R. Walko, G. Liston, C. Tremback, H. Jiang, R. McAnelly, J. Harrington, M. Nicholls, G. Carrio, et al., "RAMS 2001: Current status and future directions," *Meteorology and Atmospheric Physics* **82,** 5–29 (2003).

[73] H. Morrison and W. Grabowski, "A novel approach for representing ice microphysics in models: Description and tests using a kinematic framework," *Journal of the Atmospheric Sciences* **65,** 1528–1548 (2008).

# A Appendix

Table 2 contains all the used symbols and their explanations while Table 3 contains all the used mathematical operators. In Table 4 there are all the used abbreviations and their explanations. To make it easier to read the UCLA LES model code in Table 5 there are the variable names used in the thermodynamic module and in Table 6 there are the variable names used in the microphysical module.

Table 2: **Used symbols**

| Symbol | Definition | Value | Unit |
|---|---|---|---|
| $\alpha_i$ | Constant in fall speed relation | 317.0 | $\mathrm{m\,s^{-1}\,kg^{-\beta_i}}$ |
| $\beta_e$ | Extinctien coefficient | | |
| $\beta_i$ | Constant in fall speed relation | 0.363 | |
| $\Delta t$ | Length of time step | | s |
| $\delta_{ij}$ | Kronecker delta | | |
| $\epsilon_{ijk}$ | Levi-Civita symbol | | |
| $\gamma_{\varphi j}$ | Sub-filter scale flux | | |
| $\kappa$ | Von Kármán constant | 0.35 | |
| $\lambda$ | Wavelength of radiation | | m |
| $\lambda_{sb}$ | Slope in size distribution | | |
| $\mu$ | Zenith angle | | |
| $\mu_{sb}$ | Const. in generalized $\Gamma$-dist. | $\frac{1}{3}$ | |
| $\mu_{vis}$ | Coefficient of viscosity | | |
| $\nu$ | Const. in generalized $\Gamma$-dist. | 1 | |
| $\nu_{air}$ | Kinematic viscosity of air | $1.46 \times 10^{-5}$ | $\mathrm{m^2\,s^{-1}}$ |
| $\tilde{\omega}$ | Single scattering albedo | | |
| $\omega_l^*$ | Expansion coefficient | | |
| $\Pi$ | Exner function | | |
| $\pi_0$ | Basic state pressure | | |
| $\pi_1$ | Second pressure | | |
| $\rho_0$ | Air density | 1.21 | $\mathrm{kg\,m^{-3}}$ |
| $\rho_a$ | Density of absorbing gas | | $\mathrm{kg\,m^{-3}}$ |

*Continued on next page...*

Table 2 – Continued

| Symbol | Definition | Value | Unit |
|---|---|---|---|
| $\rho_i$ | Density of ice | 931 | $\mathrm{kg\,m^{-3}}$ |
| $\Theta_0$ | Basic state potential temperature | | K |
| $\theta$ | Potential temperature | | K |
| $\theta_l$ | Liquid water potential temperature | | K |
| $\theta_v$ | Virtual potential temperature | | K |
| $\tau$ | Optical depth | | |
| $\tau_{ij}$ | Sub-filter scale stress tensor | | |
| $A_{het}$ | Const. in Bigg's [53] freezing | 0.2 | $\mathrm{K^{-1}}$ |
| $a_i$ | Const. in dimeter-mass | 0.217 | $\mathrm{m\,kg^{-\beta_i}}$ |
| $a_n$ | Coefficient of extiction | | |
| $B$ | Buoyancy | | $\mathrm{m\,s^{-2}}$ |
| $B_\nu$ | Planck intensity | | $\mathrm{W\,m^{-2}\,sr^{-1}\,Hz^{-1}}$ |
| $B_{het}$ | Const. in Bigg's [53] freezing | 0.65 | $\mathrm{K^{-1}}$ |
| $b_i$ | Const. in dimeter-mass | 0.302 | |
| $b_n$ | Coefficient of single scattering albedo | | |
| $c_p$ | Heat capacity of dry air | 1005 | $\mathrm{J\,kg^{-1}\,K^{-1}}$ |
| $C_s$ | Smagorinsky costant | 0.2 | |
| $D_{ij}$ | Resolved deformation | | |
| $D_e$ | Mean effective size of ice crystal | | |
| $D_v$ | Diffusivity of water vapor | $3.0 \times 10^{-5}$ | $\mathrm{m^2\,s^{-1}}$ |
| $F^+$ | Radiative flux upward | | $\mathrm{W\,m^{-2}}$ |
| $F^-$ | Radiative flux downward | | $\mathrm{W\,m^{-2}}$ |
| $f_\delta$ | Expansion coefficient | | |
| $g$ | Acceleration due to gravity | 9.81 | $\mathrm{m\,s^{-2}}$ |
| $I_\lambda$ | Intensity | | $\mathrm{W\,m^{-2}\,sr^{-1}}$ |
| $J_\lambda$ | Source function in radiation | | $\mathrm{W\,m^{-2}\,sr^{-1}}$ |
| $J_{het}$ | Temp. function for het. freezing | | $\mathrm{kg^{-1}\,s^{-1}}$ |
| $j_\lambda$ | Coefficient for emission and multiple scattering | | |
| $K_h$ | Eddy viscosity of heat | | $\mathrm{m^2\,s^{-1}}$ |

*Continued on next page...*

Table 2 – Continued

| Symbol | Definition | Value | Unit |
|---|---|---|---|
| $K_m$ | Eddy viscosity | | $\mathrm{m^2\,s^{-1}}$ |
| $K_T$ | Conductivity of heat | $2.5 \times 10^{-2}$ | $\mathrm{J\,m\,s^{-1}K^{-1}}$ |
| $k_\lambda$ | Mass extinction cross section of wavelength $\lambda$ | | |
| $k_\nu$ | Absorbtion coefficient | | |
| $L_v$ | Latent heat of vaporization | $2.5 \times 10^6$ | $\mathrm{J\,kg^{-1}}$ |
| $L_{iv}$ | Latent heat of sublimation | $2.834 \times 10^6$ | $\mathrm{J\,kg^{-1}}$ |
| $L_{max}$ | Maximum length of ice crystal | | m |
| $L_{min}$ | Minimum length of ice crystal | | m |
| $m_d$ | Mass of dry air per unit volume | | |
| $N$ | Brunt-Väisälä frequency | | |
| $N_{ic}$ | Number concentration of contact nucleation | | $\mathrm{m^{-3}}$ |
| $N_{Re}$ | Reynolds number | | |
| $N_{Sc}$ | Schmidt number | 0.71 | |
| $N_{Tii}$ | Intial number concentration of ice nuclei | | $\mathrm{m^{-3}}$ |
| $N_i$ | Ice crystal number concentration | | $\mathrm{dm^{-3}}$ |
| $N_{IN}$ | Ice nuclei number concentration | | $\mathrm{dm^{-3}}$ |
| $n_{CCN}$ | Number concentration of CCN | $300 \times 10^6$ | $\mathrm{m^{-3}}$ |
| $n_r$ | Rain water number concentration | | $\mathrm{m^{-3}}$ |
| $P$ | Phase function | | |
| $Pr$ | Prandtl number | 0.3 | |
| $p00$ | Constant reference pressure | 1000 | mb |
| $p_{iv}$ | Saturation vapor pressure over ice | | |
| $Ri$ | Sub-grid scale Richardson number | | |
| $R_d$ | Gas constant for dry air | 287.04 | $\mathrm{J\,kg^{-1}\,K^{-1}}$ |
| $R_v$ | Gas constant for water vapor | 461.5 | $\mathrm{J\,kg^{-1}\,K^{-1}}$ |
| $r_{c,min}$ | Minimum cloud droplet mass | $4.2 \times 10^{-15}$ | kg |
| $r_{c,max}$ | Maximum cloud droplet mass | $2.6 \times 10^{-10}$ | kg |
| $r_c$ | Cloud droplet mixing ratio | | $\mathrm{g\,kg^{-1}}$ |

*Continued on next page...*

Table 2 – Continued

| Symbol | Definition | Value | Unit |
|---|---|---|---|
| $r_i$ | Cloud ice mixing ratio | | $\mathrm{g\,kg^{-1}}$ |
| $r_{i,min}$ | Minimum cloud ice droplet mass | $1 \times 10^{-12}$ | kg |
| $r_{i,max}$ | Maximum cloud ice droplet mass | $7 \times 10^{-10}$ | kg |
| $r_{in}$ | Ice nuclei mixing ratio | | $\mathrm{g\,kg^{-1}}$ |
| $r_l$ | Total liquid condensate | | $\mathrm{g\,kg^{-1}}$ |
| $r_r$ | Rain water mixing ratio | | $\mathrm{g\,kg^{-1}}$ |
| $r_t$ | Total water mixing ratio | | $\mathrm{g\,kg^{-1}}$ |
| $r_v$ | Water vapor mixing ratio | | $\mathrm{g\,kg^{-1}}$ |
| $S$ | Magnitude of deformation | | |
| $S_\nu$ | Source function in radiation | | |
| $S_i$ | Supersaturation over ice | | |
| $T_{cd}$ | Cloud droplet temperature | | K |
| $T_m$ | Melting point of ice | 273.16 | K |
| $u_{j,g}$ | Geostrophic wind | | $\mathrm{m\,s^{-1}}$ |
| $v_i$ | Velocity of ice crystal | | $\mathrm{m\,s^{-1}}$ |
| $\bar{x}_c$ | Mean mass of cloud droplets | | kg |
| $z_b$ | Cloud base height | | m |
| $z_t$ | Cloud top height | | m |

Table 3: **Used operators.**

| Operator | Explanation |
|---|---|
| $\vec{u}$ | Vector u |
| $\widetilde{\varphi}$ | Filtered variable |
| $\bar{\varphi}$ | Reynolds average of $\varphi$ |
| $\Gamma(x)$ | Gamma function |

Table 4: **Used abbreviations and their explantion.**

| Abbreviation | Explanation |
|---|---|
| ABL | Atmospheric Boundary Layer |
| ASCOS | Arctic Summer Cloud Ocean Study |
| ARM | Atmospheric Radiation Measurement |
| BL | Boundary Layer |
| CCN | Cloud Condensation Nuclei |
| IN | Ice Nuclei |
| ISDAC | Indirect and Semi-Direct Aerosol Campaign |
| ECMWF | European Center for Medium Range Weather Forecast |
| FIRE-ACE | First International Satellite Cloud Climatology Project Regional Experiment - Arctic Clouds Experiment |
| GCM | General Circulation Model |
| IPCC | Intergovernmental Panel on Climate Change |
| IWP | Ice Water Path |
| LES | Large Eddy Simulation |
| LWP | Liquid Water Path |
| M-PACE | Mixed-Phase Arctic Cloud Experiment |
| RWP | Rain Water Path |
| SB | Seifert and Beheng model |
| SHEBA | Surface Heat Budget of the Arctic Ocean Experiment |
| TKE | Turbulent Kinetic Energy |
| UCLA LES | University of California, Los Angeles Large Eddy Simulation |

Table 5: **Variable names in thermodynamic module in UCLA LES model.**

| Variable name | Variable name in subroutine | Definition |
|---|---|---|
| nzp | n1 | Number of z points |
| nxp | n2 | Number of x points |
| nyp | n3 | Number of y points |
| a_pexnr | pp | Exner function |
| press | p | Pressure |
| a_tp | tl | Liquid water potential temperature |
| a_theta | th | Potential temperature |
| a_scr1 | tk | Diagnosed value of absolute temperature |
| pi0 | pi0 | Pressure |
| pi1 | pi1 | Pressure |
| th00 | th00 | Basic state potential temperature |
| a_rp | rt | Total water mixing ratio |
| vapor | rv | Vapor mixing ratio |
| liquid | rc | Condensate or cloud water (In this case total condensate) |
| a_scr2 | rs | Diagnosed liquid saturation vapor mixing ratio |
| a_rpp | rp | Rain mass mixing ratio |
| rsup | rsup | Supersaturation with respect to ice |
| cp | cp | $c_p = 1005\ J * kg^{-1}K^{-1}$ |
| R | R | $R_a = 287.04 J * kg^{-1}K^{-1}$ |
| Rm | Rm | $R_v = 461.5 J * kg^{-1}K^{-1}$ |
| cpr | cpr | $\frac{c_p}{R_a}$ |
| alvl | alvl | $2.5 \times 10^6\ \mathrm{J\,kg^{-1}}$ |
| ep | ep | $\frac{R_a}{R_v}$ |
| p00 | p00 | $1 \times 10^5\ \mathrm{Pa}$ |
| tmelt | tmelt | 273.16 K |

Table 6: **Variable names in microphysics module in UCLA LES model.**

| Variable name | Variable name in subroutine | Definition |
|---|---|---|
| dn0 | dn0 | Density |
| a_theta | th | Potential temperature |
| a_scr1 | tk | Diagnosed absolute temperature |
| vapor | vapor | Vapor mixing ratio |
| a_scr2 | rs | Diagnosed liquid saturation vapor mixing ratio |
| liquid | rc | Liquid water mixing ratio |
| a_rpp | rp | Rain mass mixing ratio |
| a_npp | np | Rain number mixing ratio |
| precip | rrate | Precipiration flux |
| a_rt | rtt | Total water mixing ratio tendency |
| a_tt | tlt | Liquid water pot. temp tendency |
| a_rpt | rpt | Rain mass mixing ratio tendency |
| a_npt | npt | Rain number mixing ratio tendency |
| a_scr7 | dissip | Dissipation |
| rsup | rsupp | Supersaturation with respect to ice |
| a_ricep | ricep | Cloud ice mixing ratio |
| a_nicep | nicep | Ice number concentration |
| a_nicenp | nicenp | Number of ice nuclei |
| a_ricet | ricet | Cloud ice tendency |
| a_nicet | nicet | Ice number tendency |
| a_nicent | nicent | Ice nuclei tendency |
| prc_i | prc_i | Ice preciptation flux |
| dzi_t | dzt | $1/(z_m(k) - z_m(k-1)$ |